

49  
RECEIVED

APR 22 1998

OSTI

IS-T-1833

Solidification Process in Melt Spun Nd-Fe-B Type Magnets

by

Li, Changping

MS Thesis submitted to Iowa State University

Ames Laboratory, U.S. DOE

Iowa State University

Ames, Iowa 50011

19980507 048  
[DTIC QUALITY INSPECTED 8]

Date Transmitted: February 23, 1998

PREPARED FOR THE U.S. DEPARTMENT OF ENERGY

UNDER CONTRACT NO. W-7405-Eng-82.

DISTRIBUTION OF THIS DOCUMENT IS UNLIMITED

MASTER

# DISCLAIMER

This report was prepared as an account of work sponsored by an agency of the United States Government. Neither the United States Government nor any agency thereof, nor any of their employees, makes any warranty, express or implied, or assumes any legal liability or responsibility for the accuracy, completeness or usefulness of any information, apparatus, product, or process disclosed, or represents that its use would not infringe privately owned rights. Reference herein to any specific commercial product, process, or service by trade name, trademark, manufacturer, or otherwise, does not necessarily constitute or imply its endorsement, recommendation, or favoring by the United States Government or any agency thereof. The views and opinions of authors expressed herein do not necessarily state or reflect those of the United States Government or any agency thereof.

This report has been reproduced directly from the best available copy.

## AVAILABILITY:

To DOE and DOE contractors: Office of Scientific and Technical Information  
P.O. Box 62  
Oak Ridge, TN 37831

prices available from: (615) 576-8401  
FTS: 626-8401

To the public: National Technical Information Service  
U.S. Department of Commerce  
5285 Port Royal Road  
Springfield, VA 22161

## TABLE OF CONTENTS

INTRODUCTION	1
LITERATURE REVIEW	9
EXPERIMENTAL PROCEDURES AND METHODS	14
Processing Techniques	14
Characterization and Sample Preparation	16
Experimental Methods	20
RESULTS AND DISCUSSION	22
Microstructural Development of Melt Spun Stoichiometric Nd-Fe-B	22
Generalized Solidification Model	36
Solidification Process in the Melt Spun 2-14-1 Alloys	41
C-axis Texturing	46
TiC Modified 2-14-1 Solidification	62
CONCLUSIONS	76
REFERENCES	80
ACKNOWLEDGEMENTS	86

## ABSTRACT

A generalized solidification model has been developed based on a systematic investigation on the microstructure of melt spun Nd-Fe-B alloys. Melt spinning was conducted on initial stoichiometric and TiC added Nd<sub>2</sub>Fe<sub>14</sub>B (2-14-1) compositions to produce under, optimally and over-quenched microstructures. Microstructural characterization was carried out by TEM, SEM, Optical microscopy, XRD, DTA, VSM and DC SQUID techniques. By taking the dendritic breakup during recalescence into consideration, this generalized model has successfully explained the solidification process of the melt spun Nd-Fe-B alloys. Challenging the conventional homogeneous nucleation models, the new model explains the fine and uniform equiaxed 2-14-1 microstructure in optimally quenched ribbons as a result of the breakup of the 2-14-1 dendrites which nucleate heterogeneously from the wheel surface and grow dendritically across the ribbon thickness due to the recalescence. Besides this dendritic breakup feature, the under-quenched microstructure is further featured with another growth front starting with the primary solidification of Fe phase near the free side, which results in a coarsely grained microstructure with Fe dendritic inclusions and overall variation in microstructure across the ribbon thickness. In addition, because a epitaxy exists between the Fe phase and the 2-14-1, the so-formed coarse 2-14-1 grains may be textured. C-axis texturing was observed in under-quenched ribbons. As a constraint to solidification models in this system, the cause and characteristics of this phenomenon has been studied in detail to test our proposed model, and agreement has been found. An extension has also been made to understand the solidification



process when TiC is added, which suggests that Ti and C slow down the growth front of both Fe and 2-14-1 phase.

## INTRODUCTION

Permanent magnets (also called hard magnets) have long occupied a prominent position in technology. Applications of a permanent magnet can be broadly categorized based on the fields in which it serves. These fields include electromechanical devices, mechanical force and torque devices, electron and ion-beam control, and medical applications<sup>1</sup>. Among a prodigious variety of products employing permanent magnets are televisions, telephones, computers, videocassette recorders, radio systems, household appliances, and automobiles<sup>2</sup>. Their many applications in a modern passenger automobile are shown in Figure 1<sup>2</sup>. Permanent magnetic materials by definition are materials that remain permanently magnetized after the application of a magnetic field, the study of which is driven by the economics, the permanent magnet market is expected to increase in value to \$6.5 billion by the year 2000<sup>1</sup>.

There are three major types of permanent magnetic materials currently being produced, specified as hard ferrites, Alnicos (Fe-Al-Ni-Co) and rare-earth alloys (Nd-Fe-B and Sm-Co). Characterized by including both 3d transition metal and 4f rare earth elements, the rare earth alloys have an excellent combination of high saturation magnetization from the 3d sublattice and huge magnetocrystalline anisotropy due to the 4f sublattice. They have shown outstanding permanent magnetic properties and been dominating the market for high performance permanent magnets since their first appearance in the early 1970s, as can be seen from Figure 2<sup>3</sup>.

With the extremely high maximum energy product, these rare-earth alloys offer the

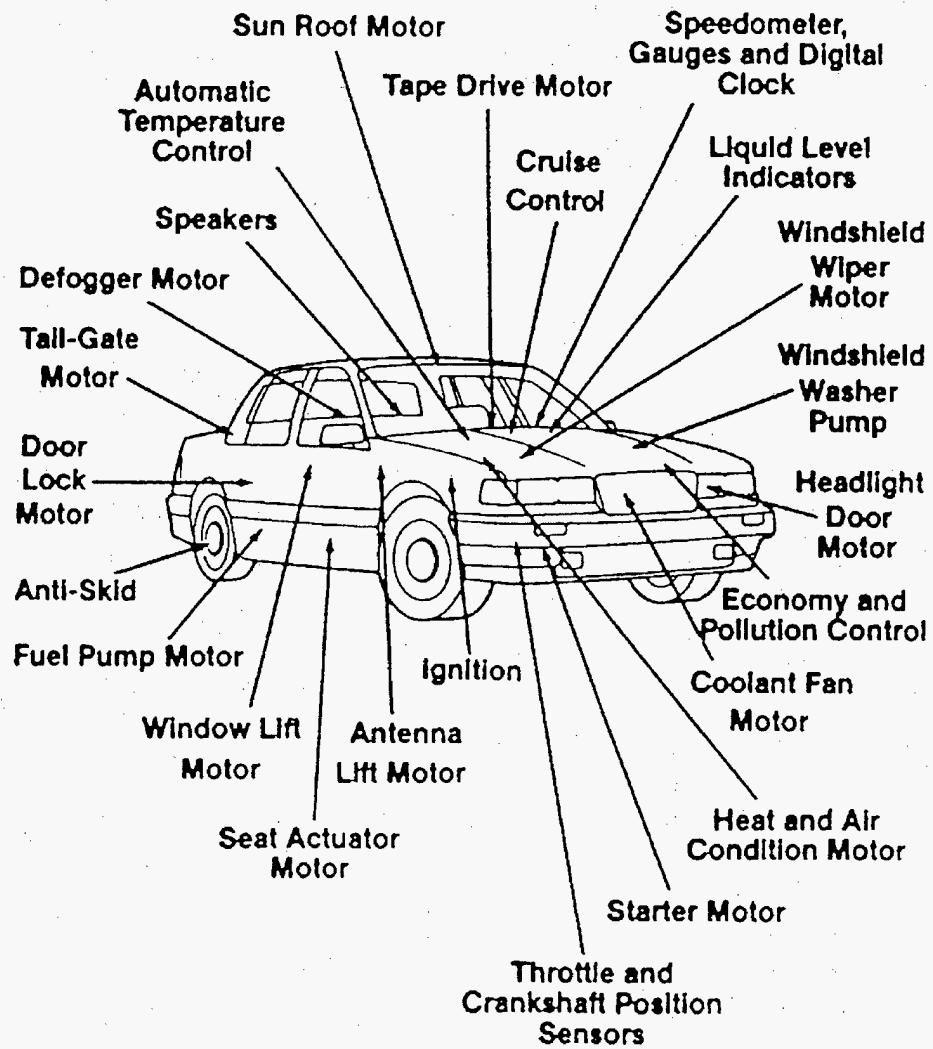


Figure 1 Automobile applications involving permanent magnets<sup>2</sup>

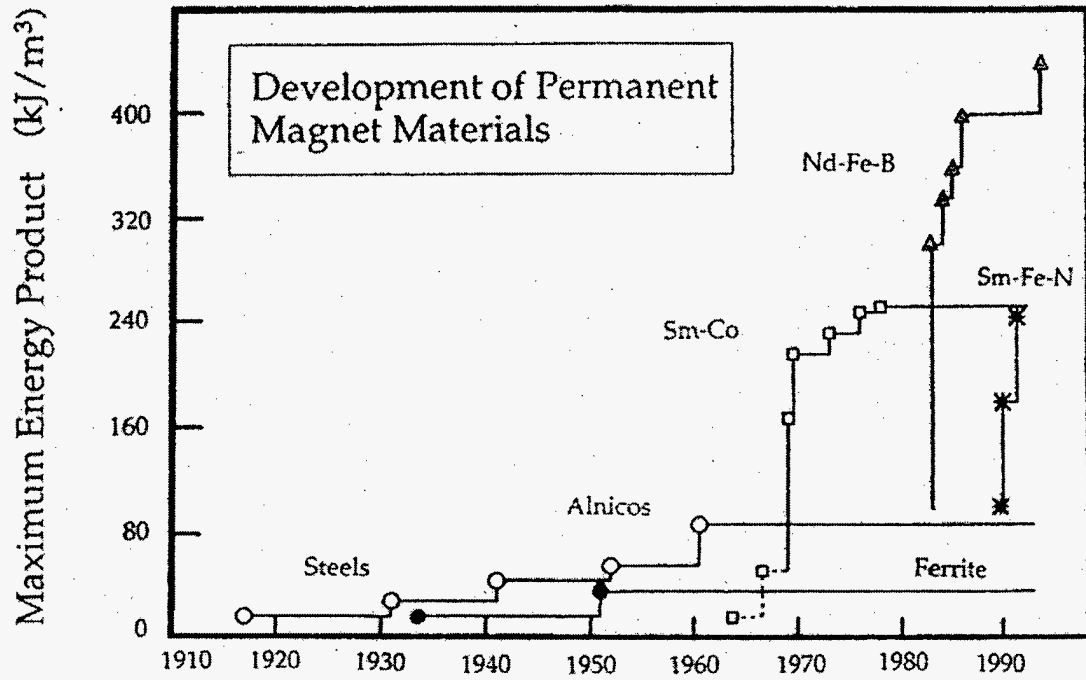
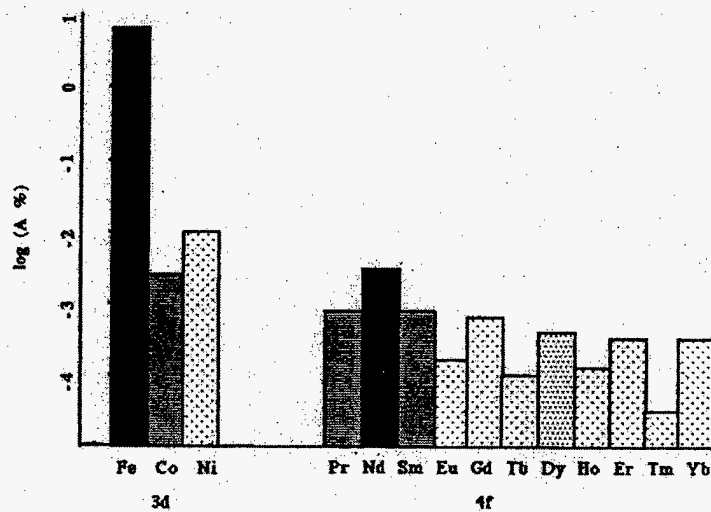


Figure 2 Energy product evolution of permanent magnets during the twentieth century<sup>3</sup>.

Energy product has increased exponentially, doubling every 12 years.

advantages of increased operation efficiency and reduction in size and weight. It is these advantages that intensify the searching and studying among these rare-earth alloys. Elements in the first half of the 4f series, the light rare-earths, are preferred in the manufacturing of the rare earth magnets due to their crustal abundances comparable to those of zinc and lead as shown in Figure 3a, and their exchange coupling with the ferromagnetic 3d elements which leads to parallel alignment of the 3d and 4f elements. Unfortunately, only strong positive 4f-3d coupling can sustain the 4f-sublattice magnetization, and thus keep the strong 4f anisotropy well above room temperature. Therefore, only Pr, Nd and Sm elements appear promising to fill the 4f sublattice, as indicated in Figure 3b, and it has been a long standing goal of the permanent magnet industry to develop a light rare earth-iron based permanent magnet.

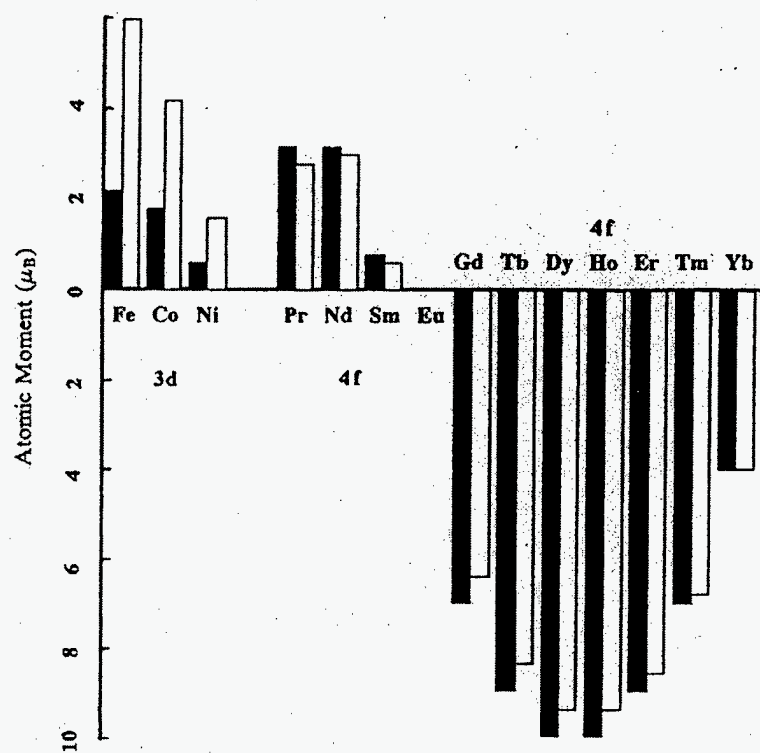
The discovery of  $\text{Nd}_2\text{Fe}_{14}\text{B}$  phase in 1983 at 29<sup>th</sup> MMM conference<sup>4-5</sup> has kindled considerable interests both technologically and scientifically in Nd-Fe-B type magnetic materials. Stabilized by B atoms, the  $\text{Nd}_2\text{Fe}_{14}\text{B}$  (2-14-1) is a stable line compound with the tetragonal structure, it has excellent combination of permanent magnetic properties including a huge uniaxial magnetocrystalline anisotropy and a saturation magnetization of over 16 KG, implying a theoretical maximum energy product of up to 64 MGOe<sup>6-7</sup>--the highest known so far. It is these attractive permanent magnetic properties that not only resulted in its quick commercialization from both the melt spinning and the sintering techniques shortly after the discovery, but also they are replacing some hard ferrites and Sm-Co compounds and expanding its market at an annual growth rate of 17.5 %<sup>1</sup>. This expansion is however limited by the relatively high production cost of the Nd-Fe-B type magnets. With the cost at least an



a

Figure 3 Information about the 3d and 4f elements<sup>3</sup>:

- a. Their relative abundances in the Earth's crust. There is a rough correlation between abundance and cost, also note iron is about 40 times as abundant as the other magnetic elements together;



b

Figure 3 (continued)

- b. Atomic moments in Bohr magnetons (black bars) and magnetic moment density in arbitrary units (white bars). Positive and negative magnetic moments indicate the sense of the exchange coupling with 3d elements.

order of magnitude lower, being only about \$2/lb compared to \$85/lb for the 2-14-1 magnets in 1992<sup>1</sup>, the hard ferrites remain occupying the largest portion of the permanent magnet market. This suggests that it is necessary to significantly lower the production cost of Nd-Fe-B type magnets in order to fully exploit their excellent permanent magnetic properties, and because material cost reflects only a small portion in their manufacturing, it is potent and necessary to reduce the total cost by exploring and optimizing the manufacturing processes.

Though the magnetic properties such as the Curie temperature, the saturation magnetization and the uniaxial magnetocrystalline anisotropy are intrinsic of the 2-14-1 phase, the efficiency to which these quantities lead to good magnetic properties such as coercivity and remanence depends on the microstructure of the particular materials, and these properties are called the extrinsic properties. This suggests a very critical role of the microstructure control in the manufacturing of a permanent magnet, and the microstructure-property relationship has long been the subject of intensive research. Furthermore, although attractive magnetic properties in the 2-14-1 system have been developed through the trial and error strategy and a variety of microstructures have been produced and reported, the origin of various microstructures, especially in the melt spun 2-14-1 alloys, remains untouched. Few people have tried to investigate the solidification process based on which various microstructures in this system had been formed. This is our first attempt in this project to take the "art"<sup>8</sup> out of the 2-14-1 manufacturing practice. This research may not directly produce a magnet with more advanced magnetic properties, however, the understanding of the solidification process may lead to better controlling of the 2-14-1 microstructures formed and developing desired microstructures for specific applications.



Besides the technological importance, our effort to understand the solidification process during melt spinning of the 2-14-1 alloys may open the door to understand the off-equilibrium solidification process of the entire peritectic system, since 2-14-1 phase is a peritectic reaction product ( $L + \gamma\text{-Fe} \rightarrow 2\text{-14-1}$ ). It is our hope that this project may benefit the ongoing research efforts worldwide to understand the peritectic solidification.

## LITERATURE REVIEW

Research efforts<sup>9-19</sup> have contributed to the development of a variety of approaches to manufacture Nd-Fe-B type magnets aside from the original sintering of fine powders and the melt spinning of molten alloys. The new techniques include the inert gas atomization<sup>9-10</sup>, mechanical alloying<sup>11-12</sup>, liquid dynamic compaction (LDC)<sup>13-14</sup> and casting based hot extrusion<sup>15-16</sup>, hot working<sup>17-18</sup> and Hydrogen Disproportionation Desorption Recombination (HDDR)<sup>19</sup> etc. processes. Energy products as high as 10 MGOe have been reported from all these routes, though they all have the potential to be commercialized, none of them has so far been commercially developed. Being one of the two established processing routes, the powder metallurgy route, which is also used for Sm-Co magnets, starts with ingots which are milled to a fine powder composed of monocrystalline particles a few microns in size, then pressed, sintered and finally heat treated to develop a desired microstructure. Dense bulk magnets can thus be produced by taking advantage of the low-melting Nd-rich intergranular phases, and an anisotropic magnet can be produced by simply adding a magnetic alignment step prior to the pressing and sintering<sup>20-21</sup>. The major advantage of the powder metallurgy is that a wide variety of sintered shapes can be produced and machined to their final tolerances. Its major disadvantage is that the monocrystalline Nd-Fe-B powders are very reactive and oxidize readily, particularly in damp environment, which means the powders have to be produced and handled in a controlled environment and this increases the processing cost significantly. The melt spinning process, on the other hand, is based on rapid solidification. In the melt spinning, a stream of molten alloy is directed and quenched on the surface of a

rotating copper (or steel) wheel. The so-obtained powder can thus be used either directly for bonded magnets, or for fully dense intermetallic magnets after subsequent hot-pressing. Anisotropic dense magnets (MQ 3) with energy product of about 50 MGOe have been developed by the hot-deforming (also called die-upsetting) process, which allows lateral plastic flow to align c-axis of 2-14-1 grains along the pressing direction. Recently, HDDR process has also been used to produce anisotropic powder from the melt spinning route<sup>22</sup>. However, one of the most cost-effective means<sup>3</sup> of producing anisotropic, fully dense Nd-Fe-B magnets would be to cast them directly into slabs with a fine grain size and with the c-axis of the grains aligned perpendicular to the surface of the slab, though it has not produced highly aligned anisotropic magnets because there is always a more or less random c-axis orientation in the plane at right angles to the predominant cooling direction. A similar effort has also been intensively directed toward producing anisotropic ribbons straight from the wheel in the melt spinning process, as this may greatly increase the magnetic properties such as the remanence. Unfortunately, this has not proved possible, although some encouraging results were reported by Coehoorn and Duchateau<sup>23</sup> who produced melt spun ribbon flakes exhibiting a pronounced c-axis texture normal to the surface of the flakes at the free side but a much weaker texture on the wheel side.

Improvement on the magnetic properties of Nd-Fe-B type magnets has benefited from intensive investigations on alloying (substituting Nd, Fe and B or adding other elements)<sup>24-40</sup>. Although it is known that no element can be beneficial to all of the permanent magnetic properties, improving one comes with the tradeoff of deteriorating some others, the alloying is practically important because not all the properties are necessary for a particular

application. All rare earth elements from Ce to Lu may substitute for Nd. Heavy rare earth substitution such as Dy and Tb<sup>24-25</sup> for Nd enlarges the intrinsic coercivity ( $H_{ci}$ ) due to the increase in anisotropy, and deteriorates the remanence at the same time. Small Dy addition<sup>26</sup> has been proved particularly useful for improving coercivity, and is essential to expand the operating temperature of the 2-14-1 magnets to 150°C or even 200°C<sup>24</sup>. Light rare earth element, Pr for example, can completely substitute Nd because of their similarity, resulting in an increase in  $H_{ci}$  due to strong coupling between Pr and Fe atoms yet a decrease in the remanence since the coupling is anti-parallel<sup>27</sup>. Transition metal Mn, Ni and Co can all substitute Fe, but Mn<sup>28</sup> and Ni<sup>29</sup> substitutions generally impair the magnetic properties. Co substitution for Fe monotonically increases the Curie temperature and thermal stability of the magnetic properties, especially the remanence, with impaired coercivity at room temperature. Therefore, Co is usually added with some other effective coercivity improving elements such as Dy<sup>24</sup>, or V and Mo<sup>30</sup>. Improvement on coercivity has also been achieved by adding Nb<sup>31</sup>, Mo<sup>32-33</sup>, V<sup>34-35</sup>, Al<sup>36-37</sup>, Ga<sup>38,35</sup>, Cu<sup>33</sup> and Ti<sup>39</sup> elements, all these additives are generally considered to affect the microstructure in a twofold way of either precipitation within the hard magnetic 2-14-1 phase or formation of new grain boundary phases. Recent progress on both the coercivity and the remanence has been made by Branagan et al.<sup>8,40</sup> by adding Ti, C two elements together.

Because those permanent magnetic properties including remanence, coercivity and energy product are extrinsic and thus highly microstructure dependent, research toward the understanding of microstructure—property relationships<sup>41-52</sup> has been a focus since the discovery of the 2-14-1 phase, and based on which, the permanent magnetic properties of the

Nd-Fe-B type magnets are moving rapidly toward its theoretical upper limits. Roughly speaking, commercial Nd-Fe-B type magnets are made richer in Nd and B compared to the  $\text{Nd}_2\text{Fe}_{14}\text{B}$  stoichiometry to suppress the primary Fe formation and form a Nd-rich grain boundary phase, which decouples the magnetization of the adjacent 2-14-1 grains during domain reversal and is thus essential to develop high coercivities. The optimum microstructure of a sintered magnet consists of the 2-14-1 phase with the grain size of 3-20  $\mu\text{m}$ <sup>8,47,48,53</sup>, which is separated by a thin layer of eutectic  $\text{Nd}_{1.1}\text{Fe}_4\text{B}_4$  intergranular phase of about 10-20 nm thick. The optimum microstructure of the melt-spun Nd-Fe-B ribbons has finer 2-14-1 grains (20-100 nm)<sup>2,47,52</sup> separated by a thin layer of Nd-rich intergranular phases, among which one was identified as  $\text{Nd}_7\text{Fe}_3$  phase<sup>51</sup>. It can be developed either through optimally quenching at a wheel speed close to 19m/s, or through suitably annealing an overquenched melt spun precursor. High coercivity can be achieved by maintaining the fine grain sizes and dispersing an effective intergranular phase as a barrier to domain wall motion. Aside from the phases present, grain size and size distribution, degree of alignment is also crucial to develop high remanence. Though magnetization reversal mechanism is still open to debate, it is generally believed that the prevailing mechanism in the sintered Nd-Fe-B magnets is nucleation-controlled<sup>53-54</sup>, and consisting of single-domain grains (the domain size is about 0.3  $\mu\text{m}$ <sup>55</sup>), the reversal mechanism in the melt spun Nd-Fe-B magnets is perceived to be pinning-controlled<sup>56-57</sup>.

Although energy products close to 50 MGOe, which is about 75% of the theoretical limit of the  $\text{Nd}_2\text{Fe}_{14}\text{B}$  compound, have been developed in laboratory from both the sintering and the melt spinning routes, space is still left in the melt spinning process to be further

exploited. Hot-deformed melt spun magnets have shown the highest energy product produced so far. The material consists of fine platelet-shaped grains of 2-14-1 phase, stacked together such that their flat faces are normal to the press direction, and these grains are also oriented in such a way that the c-axis is normal to the platelet surface<sup>49</sup>. These platelets are roughly 100-160 nm in diameter with a thickness of about 20-40 nm, and this size effect suggests a demagnetizing factor of about 0.7<sup>58</sup>. Therefore, the hot deforming process has its own disadvantage when used to produce fully dense anisotropic Nd-Fe-B magnets from the melt spinning route, because the shape of the so-formed grains is not ideal for the development of the magnetic properties. Though enormous efforts have been put into investigating the post treatment processes, little attention has been paid to the melt spinning except knowing the fact that the microstructure is very sensitive to the wheel speed. It is our purpose in this research to study the melt spun microstructure in an attempt to further exploit the potential of the melt spinning process. Being currently used as a rapid solidification process (RSP) to achieve grain refinement and amorphization in the manufacturing of high energy product Nd-Fe-B magnets, the melt spinning has also the advantage of combining RSP and directional solidification in some quenching regions. It is this character of the melt spinning that leads to texturing phenomenon in 2-14-1 melt-spun ribbon flakes. A study on this phenomenon will benefit the understanding of the solidification process during melt spinning, and practically not only is it an effective way to produce anisotropic magnets directly from the melt spinning, but also it may have great potential in the application of high-quality perpendicular recording media, with the similar morphology as the Alumite<sup>59</sup> yet much better magnetic properties.

## EXPERIMENTAL PROCEDURES AND METHODS

### Processing Techniques

#### Arc-Melting

Alloys were prepared from the elements with a lab built arc-melter. Arc-melting is a process where elements are melted on a water cooled copper hearth with electrons, and was used now as a preprocessing technique to obtain homogeneously alloyed ingots. All arc-melting was done under UHP argon, and each ingot was melted, flipped and remelted 4 times to minimize macro-segregation in the as-cast ingot. Samples were weighed before and after arc-melting and only saved if the weight loss was  $\leq 0.2$  wt.%.

#### Melt-spinning

Melt-spinning (in Figure 4) was used as the primary processing technique. Through melt-spinning, an alloy can be rapidly quenched at cooling rates up to  $10^6$  °C/s<sup>60</sup>. The quenching rate could be changed by changing the wheel tangential velocity, to a first approximation, the mean cooling rate in the vicinity of the solidification point varies linearly with the wheel tangential velocity (wheel speed)<sup>61</sup>.

The exact cooling rate achieved at a constant wheel speed depends on a number of parameters. Shooting pressure and temperature, chamber gas and pressure, crucible orifice diameter, distance above the wheel, and wheel material all have effects on the cooling rate. Melt spinning was performed with a lab built melt spinner by inductively heating an

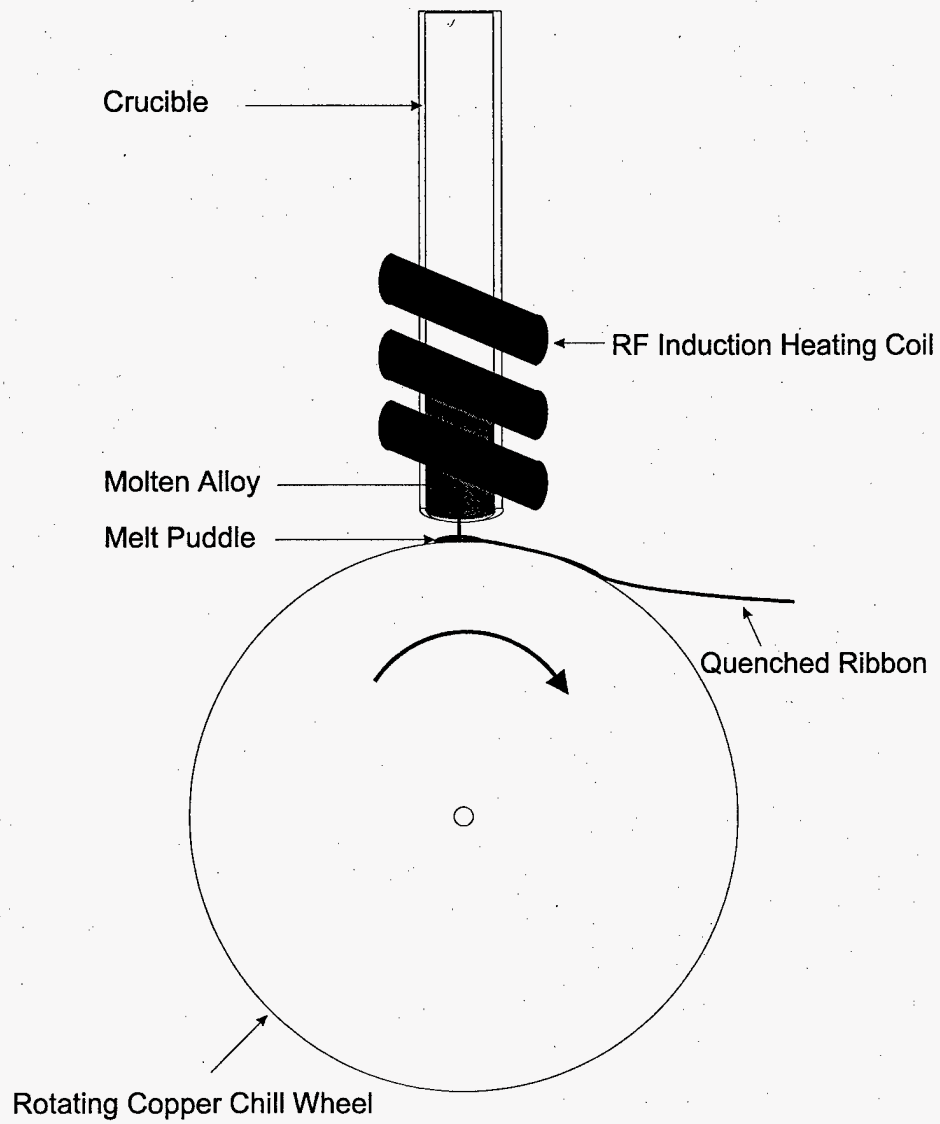


Figure 4 Schematic diagram of a melt spinner (courtesy of Kevin Dennis)



arc-melted ingot in a quartz crucible in a UHP argon atmosphere to 1375°C unless specified. The melt was ejected through an orifice of 0.81 mm diameter ~6 mm above onto a rapidly rotating copper wheel with a 150 Torr over-pressure of UHP argon. By holding as many of the melt spinning parameters as possible, reproducible and consistent cooling rates were obtained at a particular wheel speed.

## **Characterization and Sample Preparation**

A variety of characterization techniques were used in this project. The sample preparation and operating conditions were standardized as far as possible for the parallel comparisons, furthermore, different sample preparation procedures for each technique were used to maximum the information we can get from each sample.

### **Transmission Electron Microscopy**

Transmission Electron Microscopy (TEM) is a microscopy technique where electrons are transmitted through the sample. Images can be obtained through the bright field (BF) and dark field (DF) modes according to the electrons used for imaging. A BF image is formed from the directly transmitted beam, and a DF image is formed in an opposite manner through imaging a set of diffracted electrons, which is very useful to study grain orientations or the morphology and distribution of the grains of a particular phase. The TEM has a much higher resolution than the SEM, and has the capacity of collecting structural information in Selected Area Diffraction (SAD) mode from a region as small as ~1  $\mu\text{m}$  in diameter, and further down to about 9 nm when Convergent Beam Electron Diffraction (CBED) is used. TEM is

generally equipped with Energy Dispersive Spectroscopy (EDS) and Electron Energy Loss Spectroscopy (EELS) detectors, and based on which, element identification can be easily done. The EDS can only be used to identify elements with atomic number greater than 5, and is suitable for heavy elements and also the only choice if the tested regions are too thick for electrons to penetrate. On the contrary, EELS has better spatial resolution and is more suitable for light elements' identification

TEM was performed using a Philips CM-30 microscope, which is equipped with a Link Analytical X-Ray EDS detector and a Gatan Parallel EELS (PEELS) detector. The typical operating voltage was 300 keV. The standard sample preparation procedure of a cross-sectional TEM sample is as follows: melt-spun ribbons were stacked top to bottom in a 3 mm quartz tube and epoxied with the EPO-TEK 353ND epoxy. After curing the tube was sliced forming disks of sandwiched ribbons in cross-section. These 3 mm disks were then mechanically polished to  $\sim 50 \mu\text{m}$  and argon ion-milled at 5 kv, using cold stage cooled by liquid nitrogen. When preparing a planar TEM sample, a melt spun ribbon flake was cemented onto copper disks with a 1 mm hole, then polished and ion-milled preferentially from one side using cold stage cooled by liquid nitrogen at 5 kv.

### **Scanning Electron Microscopy**

Scanning electron microscope (SEM) is an analytical tool which uses a collimated electron beam rastered over the specimen surface. SEM was done with JOEL JSM 6100 microscope equipped with a Oxford Link Pentaset EDS system. A picture of the overall microstructural development at a large scale can be obtained due to much large imaging area

from the SEM, and the whole ribbons can be observed instead of just the very thin edges of the sample as in the TEM. Moreover, the EDS system was used to check the compositional variation across the ribbon thickness. All the SEM samples studied were made as cross-sectional samples. Melt-spun ribbons were stacked top to bottom in a 3 mm quartz tube and epoxied with the silver epoxy, after curing the tube was polished in such a way that the sandwiched ribbons are normal to the polishing plane, and the polishing was done in steps finishing with a 0.125  $\mu\text{m}$  diamond slurry. The samples were eventually etched.

### **Optical Microscopy**

Optical microscopy was used as part of the effort to complete the picture of the overall microstructural development. The same sample preparation procedure as for SEM sample was used.

### **Differential Thermal Analysis**

Differential thermal analysis (DTA) is concerned with the rate of the temperature change of a sample undergoing a constant rate of heat input. Any physical changes in the sample such as melting, crystallization, phase transformation etc. will cause heat to be absorbed or released which can be measured against an inert reference (usually  $\text{Al}_2\text{O}_3$  or  $\text{MgO}$ ).

DTA was performed on a Perkin Elmer DTA 7. Based on the change of enthalpy and the onset temperature of the crystallization events, glassy phase fraction and viscosity of the glass can be qualitatively measured. Samples were prepared by grinding melt spun ribbons in

a nitrogen glove box to  $< 50 \mu\text{m}$  in size, and weighed with a precision of 0.0001 gram. Heating rates were at  $10^\circ\text{C}/\text{min}$  with a UHP argon flow rate of 50 cc/min, and Alumina ( $\text{Al}_2\text{O}_3$ ) was used as the standard. DTA events were reported as peak onsets due to the heating rate dependence of the peak temperatures.

### **X-Ray Diffraction**

X-Ray Diffraction (XRD) was used to determine both the phase composition and development of texture formed. XRD was done on a Phillips diffractometer equipped with a vertical  $\theta/2\theta$  goniometer. Copper  $\text{K}\alpha$  characteristic radiation was filtered with a graphite monochromator and used for diffraction. The typical operating values were 40 kv and 20 mA, typical counting time and step width were 3.0 second and  $0.05^\circ$  respectively. Melt spun ribbons were ground in an argon glove box to powders  $< 50 \mu\text{m}$  when preparing powdered XRD samples. Ribbon samples were prepared by placing about 10 ribbons on a flat quartz slide, with either the wheel or free side facing up.

### **DC SQUID**

Hysteresis loops were measured using a Quantum Design DC SQUID Magnetometer at 300 K. Ribbon samples were prepared by placing about 20 ribbons parallel on a Scotch tape, the tape was then wrapped onto a quartz rod by situating the long axis of the ribbons parallel to the applied magnetic field. Powdered samples were prepared by first grinding the melt spun ribbons in an argon glove box to  $< 50 \mu\text{m}$ , then putting into a quartz tube and

freezing the powder with PTFE Thread seal tape to avoid its rotation during the measurement.

### **Vibrating Sample Magnetometer**

Vibrating Sample Magnetometer (VSM) measures the total magnetization of a sample. Based on the assumption that the free Fe phase is the only phase remaining ferromagnetic at an elevated temperature, 500 °C for example, the magnetization measured at this temperature can be used as a means representative of the free iron phase present. The VSM used was a model 4500 Princeton Applied Research VSM. It had the capability to measure samples up to 10,000 emu (electromagnetic unit) and temperatures up to 1000°C. The VSM furnace temperature was calibrated with a high purity nickel standard, and the measurements were done in the magnetic field of 1.5 T. Samples of the melt spun ribbons were first ground in an argon glove box to < 50 µm, then transported and eventually sealed in argon environment. The whole procedure was designed to ensure an oxygen free environment, and thus no oxidation or decomposition of the 2-14-1 phase occurred when heating the sample.

### **Experimental Methods**

Stoichiometric 2-14-1 was alloyed and melt spun at wheel speeds ranging from 10 m/s to 40 m/s to study the underlying solidification process. A picture of the microstructural development in the melt spun ribbons was attempted by three dimensionally imaging them. Most cross-sectional and planar microstructural information was obtained from TEM study,

SEM and Optical microscopy further helped to complete the whole picture of the microstructural development, especially the longitudinal microstructural variation. In addition, the EDS system equipped with the SEM was used to check compositional variation across the ribbon thickness. DTA and XRD were also conducted to identify the phases present and phase fractions.

Based on the understanding of the solidification process happening during the melt spinning of the stoichiometric 2-14-1, a step was made further to understand TiC modified solidification. 2 at.% TiC added 2-14-1 designed as  $(\text{Nd}_{2/17}\text{Fe}_{14/17}\text{B}_{1/17})_{96}\text{Ti}_2\text{C}_2$  was prepared by changing the wheel speed from 10 m/s to 40 m/s. The microstructural development was studied in the same way as its stoichiometric counterpart, and comparisons were made. In addition, special attention was paid to the appearance of the additives to study their effect in the solidification process using TEM, EELS, DTA etc. techniques.

As a constraint of solidification models, c-axis texturing was observed in XRD from ribbon samples. Based on the evidence obtained from the TEM, the cause of this texture was proposed. Further detailed study on the cause and characteristics of the texturing phenomenon verified our generalized solidification model. Alloys were designed by fixing the Nd:B ratio as 2:1 and changing the Nd:Fe ratio (R) from 0.114, 0.130, 0.143 (stoichiometry) and 0.160 to cover all composition range. Melt spun ribbons were produced by changing the melt spinning parameters including the wheel speed, the shooting temperature and the wheel material. These ribbons were analyzed by XRD to measure the degree of the c-axis alignment, by VSM to measure the  $\alpha$ -Fe phase formed and by SQUID to measure the effect of the texture on the magnetic properties.

## RESULTS AND DISCUSSION

### Microstructural Development of Melt Spun Stoichiometric Nd-Fe-B

Analysis of the microstructural development during melt spinning of Nd-Fe-B alloys will be based on the microstructural information obtained from three mutually perpendicular directions, namely cross-sectional (across the ribbon thickness), longitudinal and transverse directions.

The microstructure across an under-quenched 2-14-1 ribbon is highly variable from the wheel side to the free side. At low quenching rates,  $10 \text{ ms}^{-1}$  wheel speed for example, the cross-sectional microstructure is featured with 4 distinct sections, as shown in Figure 5. The wheel side section (in Figure 5a) shows a thin layer ( $\sim 0.3 \text{ }\mu\text{m}$ ) consisting of fine equiaxed 2-14-1 grains, which is followed by a thicker region ( $\sim 20 \text{ }\mu\text{m}$ ) where the equiaxed 2-14-1 grains coarsen systematically from  $< 100 \text{ nm}$  in size to about  $300 \text{ nm}$ , also in this region, there are frequently  $\alpha$ -Fe particles at triple conjunctions of 2-14-1 grains (in Figure 5b) yet no grain boundary phase has been observed. Further away from the wheel side, coarser grains up to  $1 \text{ }\mu\text{m}$  in diameter show up in another transition region, which are separated by a thin layer of Nd-rich intergranular phase, as shown in Figure 5c. This gives away to a microstructure composed of large equiaxed 2-14-1 grains ( $1\text{-}10 \text{ }\mu\text{m}$ ) with aligned  $\alpha$ -Fe inclusions when close to the free side, which is termed in this thesis as the free side microstructure, as shown in Figure 5d. These inclusions have a pinch and swell morphology and are up to  $30 \text{ nm}$  wide dendrites, identification of which comes directly from the EDS results shown in Figure 6.

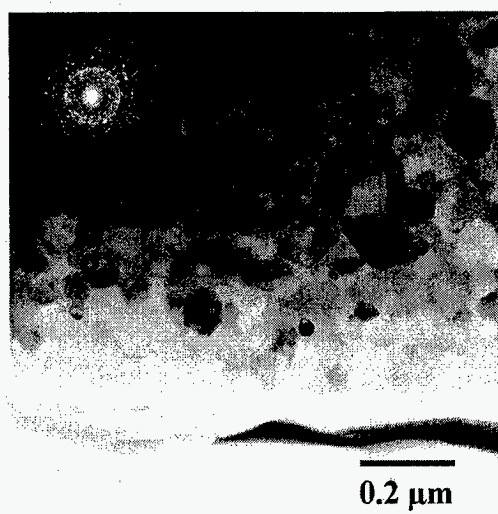
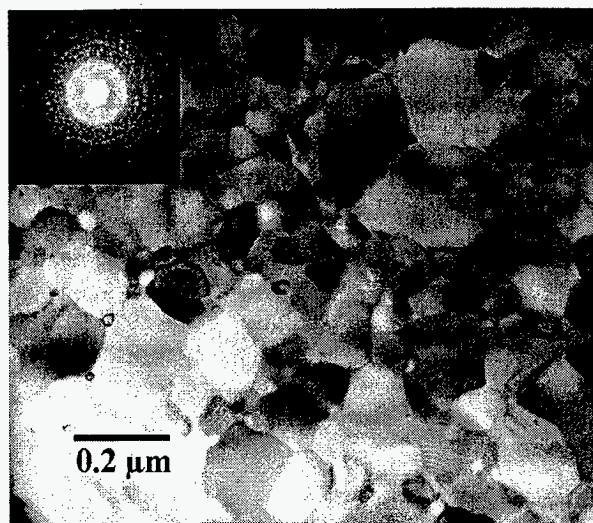
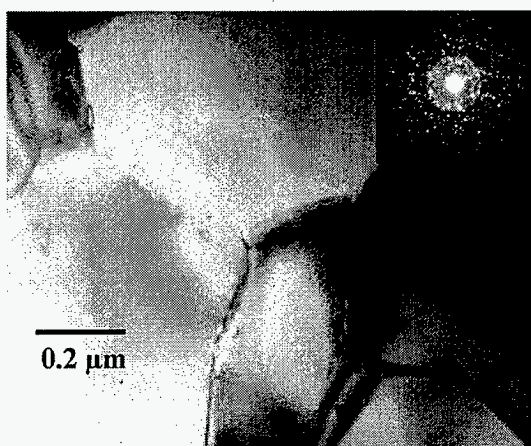
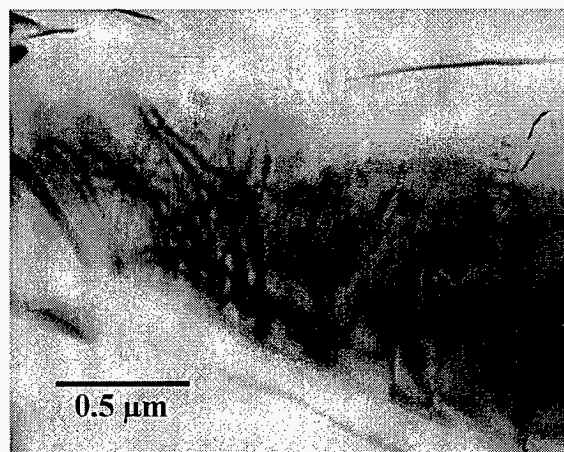
**a****b****c****d**

Figure 5 Cross-sectional TEM images of a  $\text{Nd}_2\text{Fe}_{14}\text{B}$  @  $10 \text{ ms}^{-1}$  ribbon flake:  
a. wheel side; b. transition region 1; c. transition region 2; d. free side.



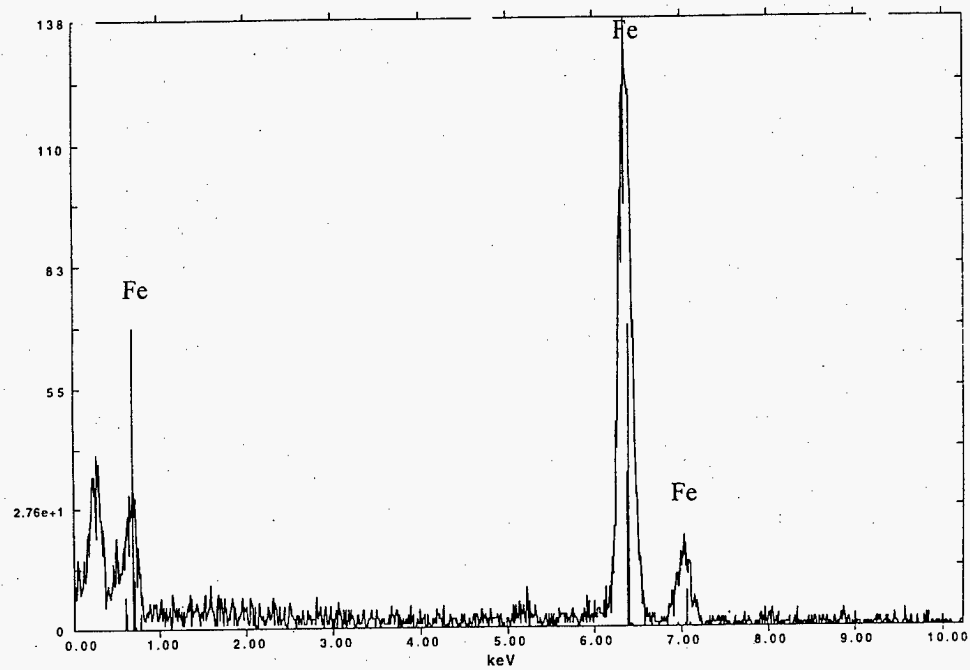
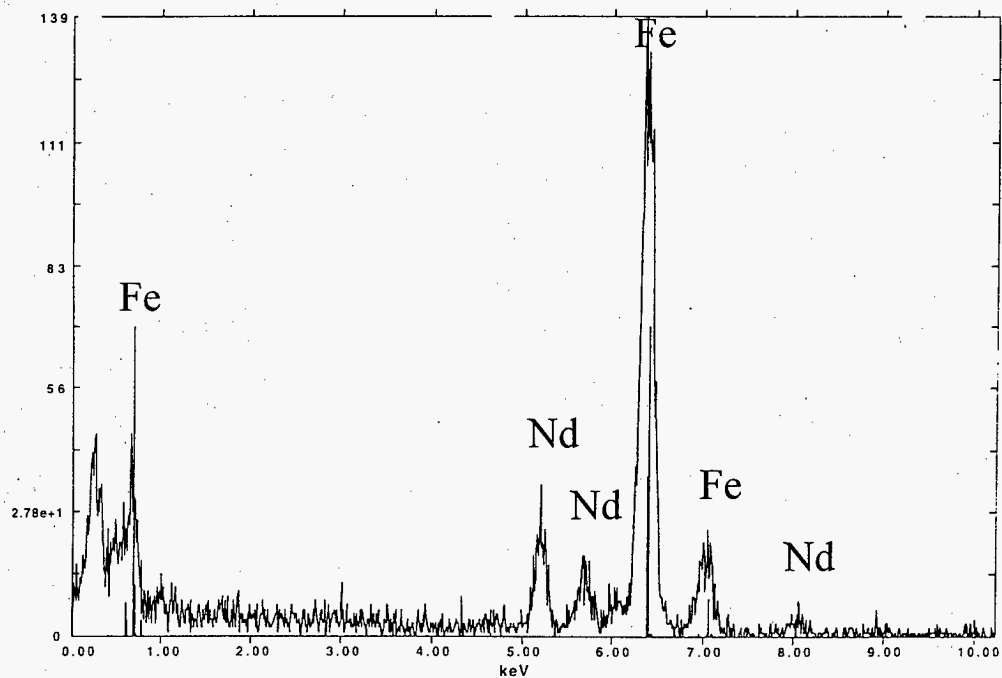
**a****b**

Figure 6 EDS results from  $\text{Nd}_2\text{Fe}_{14}\text{B}$  @  $10\text{ms}^{-1}$  ribbons on :  
a. Fe inclusions; b. the matrix

Only Fe element is obtained from the inclusions as indicated in Figure 6a, yet both Nd and Fe elements have been detected from the matrix (in Figure 6b). These 2-14-1 grains are aligned with the c-axis normal to the flat ribbon surface, and the alignment of the proeutectic (primary) iron phase appears to be the internal cause, detailed analysis will be in a special case of the solidification model being developed.

Optical microscopy and SEM study on these ribbons confirmed that the cross-sectional microstructural variation revealed in the TEM study is typical in all the under-quenched ribbons. Though all the 2-14-1 grains are equiaxed, the size change from fine to very coarse through the ribbon thickness is evident in etched ribbon samples, as can be seen from Figure 7. Also as noted, the coarsely grained regions in the figure appears to correspond to the free side microstructure as described in Figure 5d. Meanwhile, along the ribbons, the boundary separating the fine and the very coarse grains is not in the plane normal to the thermal gradient direction. It is overall irregular, and appears to be sinusoid-like curved, which is believed to be caused by the roughness of the wheel surface in such a way that the asperities on the wheel surface first contact the melt and stimulate heterogeneous nucleation there, the valleys however spend more time to contact the melt due to the liquid surface tension which impedes wetting and thus imply late nucleation events. Therefore, the interface is unevenly pushed longitudinally and transversely, and because of this, the same shaped curves should be also present in the transverse direction. Favorable evidence of the above explanation can be found in a successful attempt to relate the predendritic nuclei density to the rugosity of a bare copper mold by M. Prates and H. Biloni<sup>62</sup> 25 years ago and the "peaks and valleys" observed by Pond and Winter<sup>63</sup> in a pure tin chill block melt spun ribbon.



Figure 7 Optical image of etched Nd<sub>2</sub>Fe<sub>14</sub>B@10 ms<sup>-1</sup> ribbon flakes

This sinusoid-like curved boundary is very important in the understanding of the solidification process during melt spinning at under-quenched conditions, because it reveals that the first nucleation events are heterogeneous on the wheel side of under-quenched ribbons, which later on grow along the temperature gradient and across the ribbon thickness.

Since composition is the internal cause of the microstructure locally present, knowing the microstructure that have been developed is not enough to deduce the solidification process occurring during the melt spinning unless it holds true that the composition is evenly distributed. SEM equipped with EDS system was then used not only to obtain some highly resolved macroscopic information, but also to check the cross-sectional compositional distribution. Figure 8 shows a SEM image from some typical  $\text{Nd}_2\text{Fe}_{14}\text{B}@10\text{ms}^{-1}$  ribbons, EDS analysis results on points across the middle ribbon in the figure are listed in Table 1. As can be seen from the table, the composition across the ribbon thickness is evenly distributed, in other words, no compositional segregation is present within the experimental error.

Table 1 EDS result across a  $\text{Nd}_2\text{Fe}_{14}\text{B}@10\text{ms}^{-1}$  ribbon

(Nd % + Fe % = 100 % is assumed)

	A	B	C	D	E	F	G
Nd at. %	20	19	20	20	20	20	20
Fe at. %	80	81	80	80	80	80	80

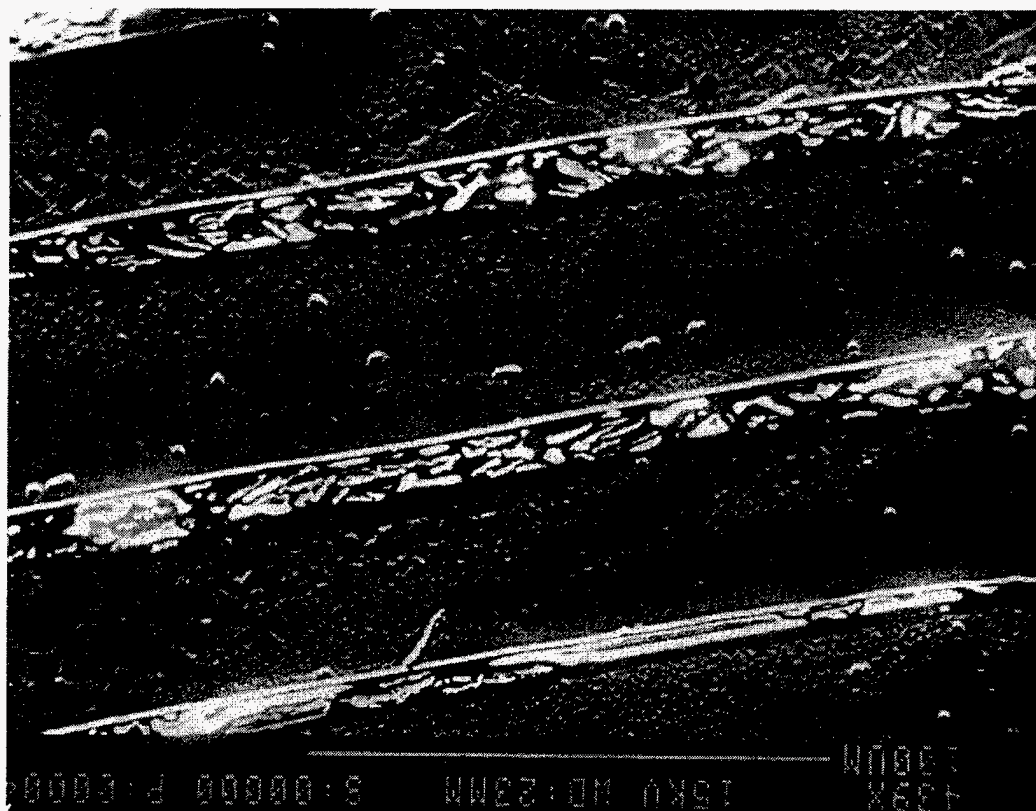


Figure 8 SEM image of 2-14-1 ribbons melt spun at 10 m/s

With the increase in wheel speeds, ribbons are made thinner and more effective quenching is achieved, meanwhile, the microstructure close to the wheel side becomes finer and eventually amorphous. When the wheel speed is increased to around 19 m/s, so-called optimally quenched microstructure becomes dominant. An example is in Figure 9, showing cross-sectional TEM images of a typical ribbon melt spun at 20 m/s ( $\text{Nd}_2\text{Fe}_{14}\text{B}@20\text{ms}^{-1}$ ). As shown in the figure, fine equiaxed 2-14-1 grains are formed from the wheel side to the free side with an average grain size of about 60 nm. These single-domain grains are the basis to develop excellent magnetic properties. An interesting feature revealed by these TEM images is the homogeneity across the ribbon, the grain size is almost the same from the wheel side to the free side. This fact seems contradictory if explaining with conventional models, because once the positive thermal gradient across the ribbon is assumed, the nucleation rates (both heterogeneous and homogeneous), which are the degree of undercooling dependent, should be different from one side to the other and thus different grain size is expected to occur.

The cross-sectional homogeneity is further confirmed by the SEM image of the same ribbon samples (shown in Figure 10), and from the points indicated on one ribbon in the figure, EDS result (in Table 2) excludes the possibility of compositional segregation. Furthermore, the microstructure appears also longitudinally uniform, and free of the optically coarsely grained microstructure as observed in under-quenched ribbons, which suggests that the more effective quenching has pushed the curved interface out of these ribbons.

$\text{Nd}_2\text{Fe}_{14}\text{B}@20\text{ms}^{-1}$  ribbons have in fact touched the category of over-quenched region provided that the two-phase microstructure consisting of nanophased and amorphous 2-14-1 is used as the definition of the over-quenched microstructure. Based on the enthalpy change

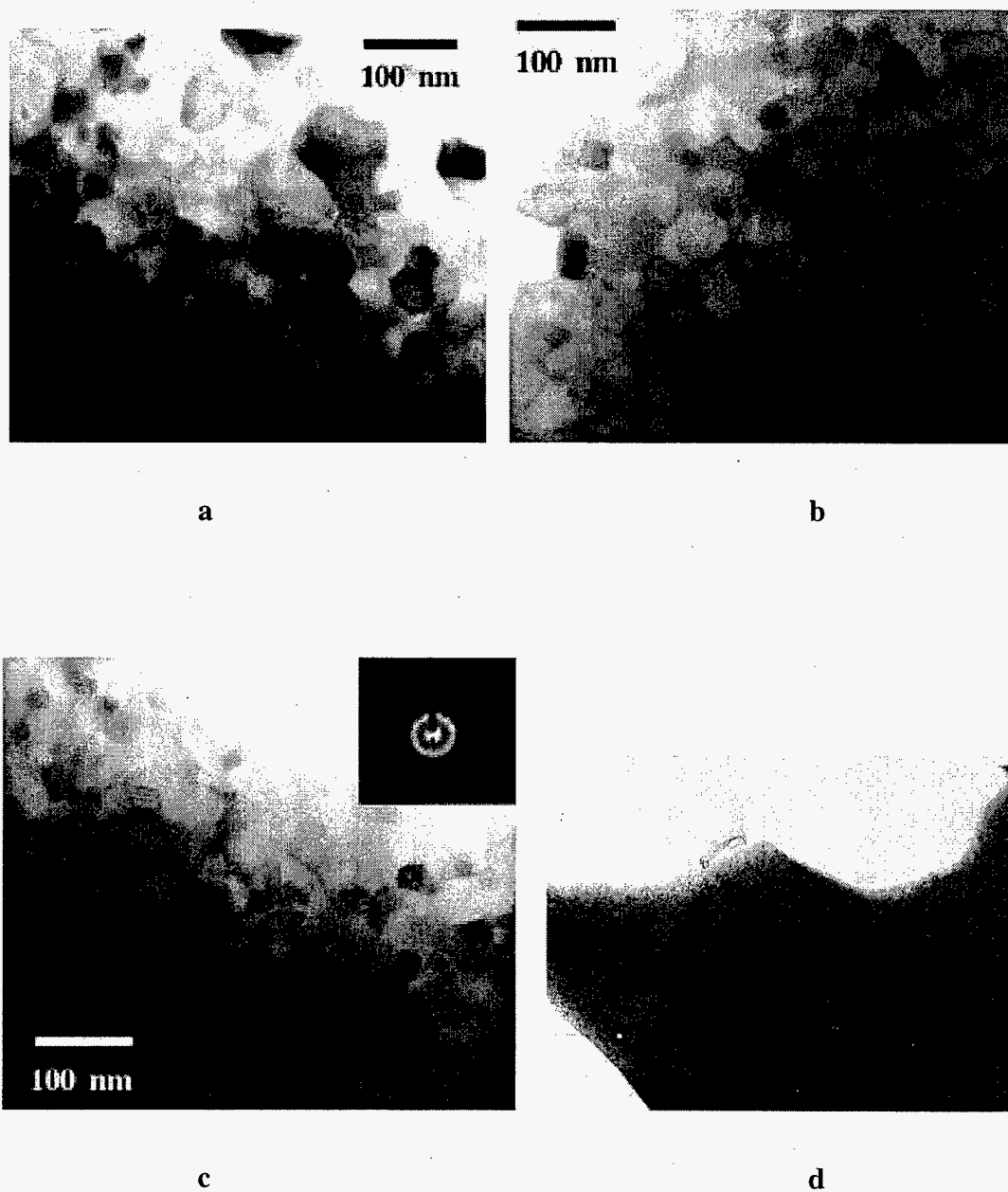


Figure 9 Cross-sectional TEM images of a  $\text{Nd}_2\text{Fe}_{14}\text{B}@20 \text{ ms}^{-1}$  ribbon :  
a. free side; b. middle region; c. wheel side; d. the ribbon profile

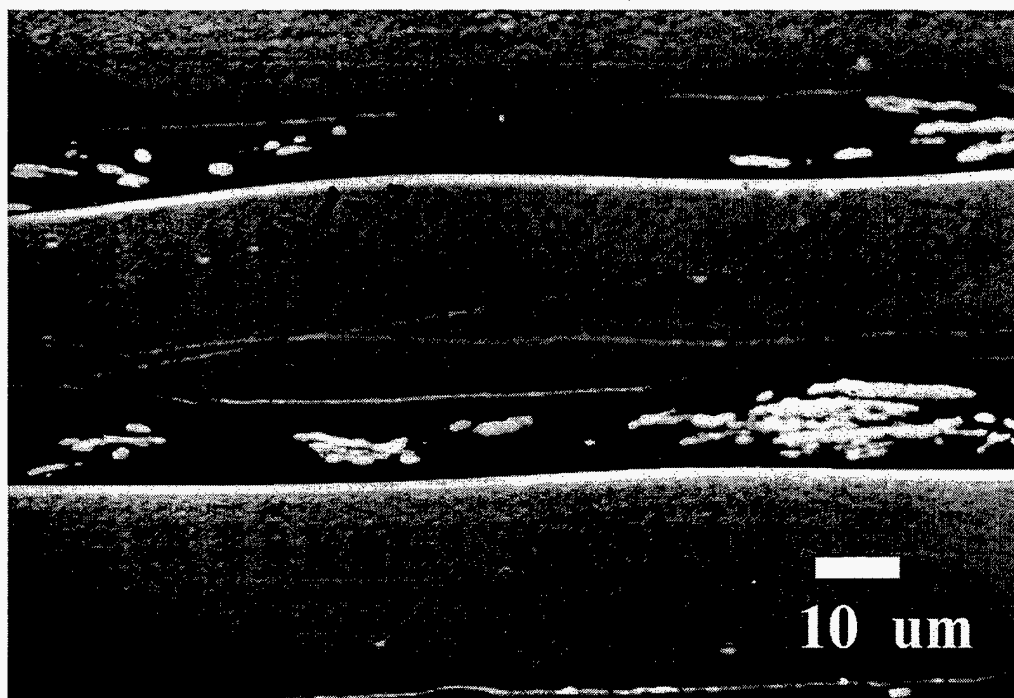


Figure 10 A typical SEM image of Nd<sub>2</sub>Fe<sub>14</sub>B@20 ms<sup>-1</sup> ribbons.



Table 2 EDS result on the  $\text{Nd}_2\text{Fe}_{14}\text{B}@20\text{ms}^{-1}$  ribbon shown in Figure 10

(Nd % + Fe % = 100 % is assumed)

	1-1	1-2	1-3
Nd at. %	21	21	21
Fe at. %	79	79	79

when heating the sample through the crystallization transformation, DTA result reveals that about 8 % (volume) glass has been formed in these ribbons. This glassy phase may reside in the grain boundary areas as very thin layers or on the very edge of the wheel side, and its occupancy of such a small volume percentage makes it hardly detectable in the TEM study. Meanwhile,  $\alpha$ -Fe particles have also been frequently observed at grain conjunctions, and this is consistent qualitatively with about 2.5 vol. % presence of the  $\alpha$ -Fe phase obtained from VSM measurements.

Further increase in wheel speeds produces microstructures with finer crystalline 2-14-1 and more phase fractions of glass. For ribbons melt spun at 30 m/s, amorphization has been achieved in over half of the ribbon volumes-- about 70 vol. % of glass measured from DTA experiments. Microscopically, wheel side microstructure is 100 % glass and crystallized 2-14-1 phase can only be found in regions close to the free side, which is separated by 2-14-1 intergranular glass, as shown in Figure 11.

Amorphization spreads the whole ribbon once the wheel speed has reached 40 m/s, featureless microstructure is predominant across a  $\text{Nd}_2\text{Fe}_{14}\text{B}@40\text{ms}^{-1}$  ribbon and the glassy matrix has been identified by XRD, Selected Area Diffraction Pattern (SADP) and DTA

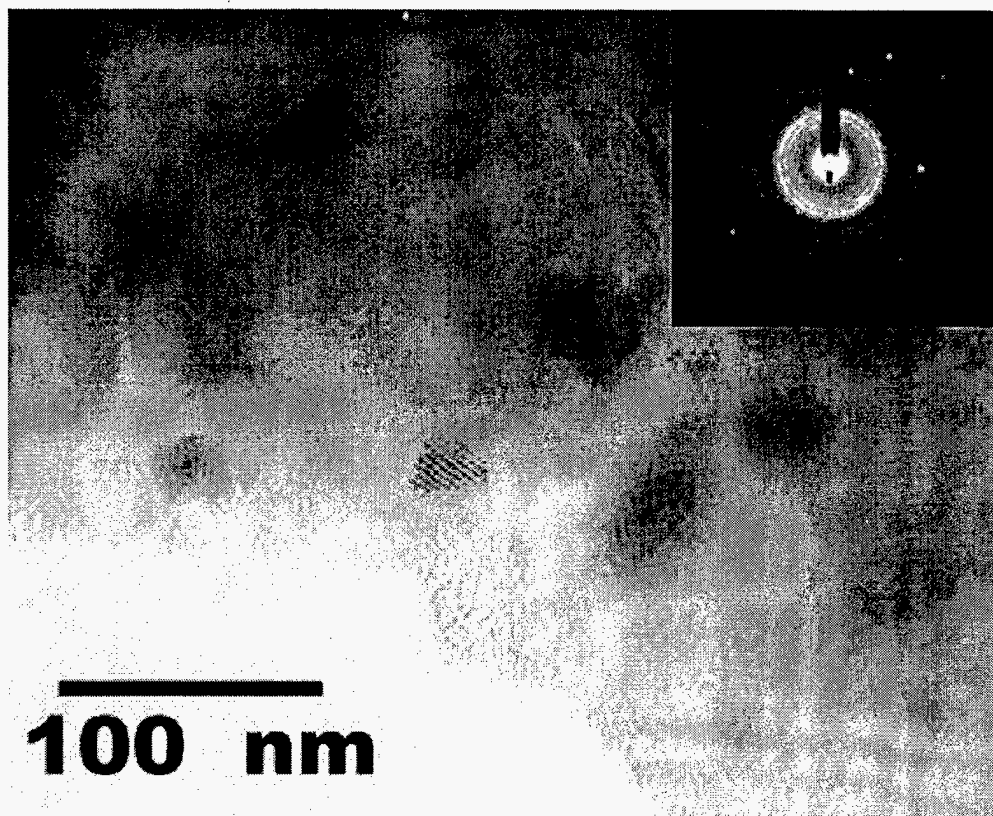
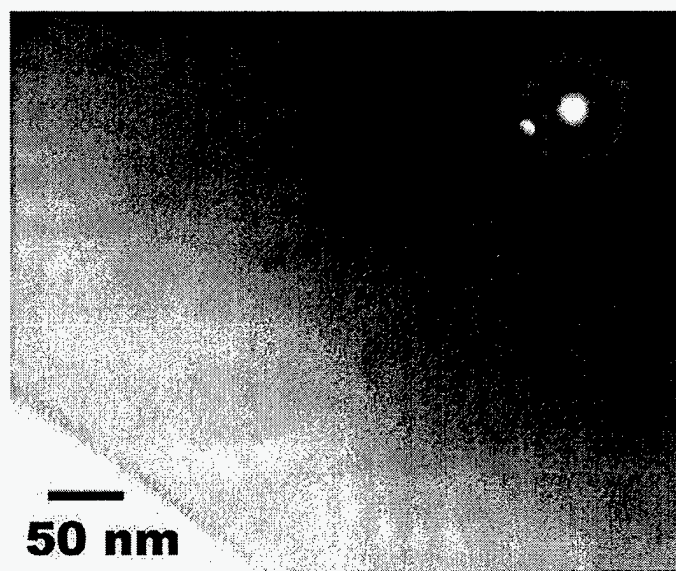


Figure 11 TEM image of crystallized region in 2-14-1 ribbons melt spun at 30 m/s.

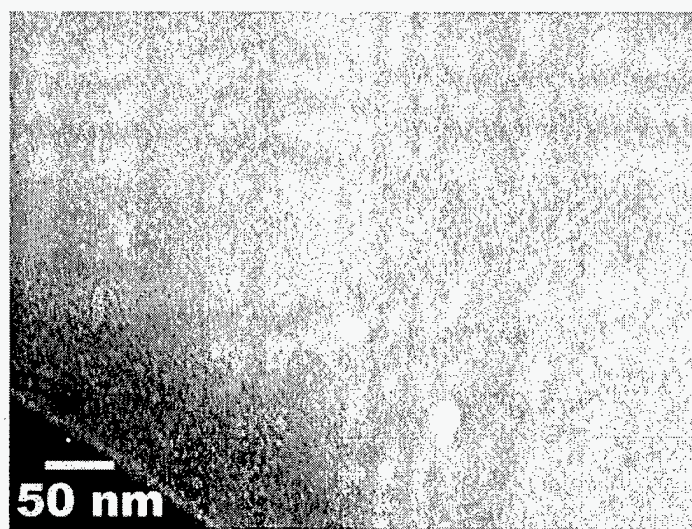
techniques. Meanwhile, nuclei have also been observed and by comparing the Bright Field (BF) and Dark Field (DF) images taken from the same region, as shown in Figure 12, and the identification of these two nuclei as 2-14-1 phase is based on the information from the Convergent Beam Electron Diffraction (CBED) inserted.

It should be noted however that the melt spinning process becomes less stable at high wheel speeds. One result from this instability is the formation of some “pocketed” or “trapped” regions, where the quenching rate is lower than what is expected from the wheel speed used.

Microstructure from the quenching rates generally used in the melt spinning process have so far been studied by changing the wheel speed of copper from 10 m/s to 40 m/s, yet it may be easier to begin our understanding of the underlying solidification process with some simpler cases which are more under-quenched and thus closer to the equilibrium situation. Although theoretically a wide range of quenching rates can be achieved by continuously lowering the wheel speed, fusion between ribbons becomes so severe at low speeds ( $< 5$  m/s) and therefore is not reliable. Fortunately, lower quenching rate than what we have shown had been achieved by using a steel wheel<sup>64</sup>, and a microstructure beginning with the equiaxed grains at the wheel side and columnar 2-14-1 grains across the ribbon was formed. The reason of lower quenchability when substituting the copper wheel with a steel wheel lies in the fact that steel has a relatively poor thermal conductivity of  $0.8 \text{ W.cm}^{-1}.\text{K}^{-1}$ , just about one fifth of that of copper. This effect has also been verified by measuring the change of glassy phase fraction with wheel speeds using 6 at. % TiC added 2-14-1 alloys, the slope of this curve has been greatly flattened when a steel wheel is used. A standard explanation for



(a)



(b)

Figure 12 TEM images of over-quenched ribbons showing 2-14-1 nuclei in glassy matrix: (a) BF image; (b) DF image

this microstructure is similar to those low freezing alloys, Fe-6.5 wt.% Si for example, it is generally believed that the solidification during the melt spinning begins with heterogeneous nucleation of the undercooled liquid on the wheel surface, followed by columnar growth through the ribbon thickness due to the dominant positive thermal gradient.

Further under-quenching, a quasi-equilibrium microstructure can be produced in the casting with copper mold<sup>65</sup>, which consists of dendritic  $\alpha$ -Fe inclusions within 2-14-1 grains, and these dendrites reach about 100  $\mu\text{m}$  length in the primary growth direction. This microstructure is considered to be caused by the equilibrium peritectic reaction  $L + \text{Fe} (\gamma\text{-Fe}) \rightarrow 2\text{-14-1}$ . During the casting, properitectic Fe ( $\gamma\text{-Fe}$ ) phase nucleates heterogeneously from the mold whenever the melt has been cooled down to below the liquidus temperature ( $T_l$ ) and grows dendritically in the direction of the thermal gradient. This growth is then replaced by nucleation of the 2-14-1 phase from the properitectic iron dendrites when cooled to below the peritectic temperature ( $T_p$ ), and the 2-14-1 phase grows outwards by continuously consuming the properitectic iron and solid state diffusion of iron atoms through the solidified layer. The 2-14-1 phase theoretically should be the only phase left in the equilibrium microstructure of stoichiometric composition, most cases are however off-equilibrium and  $\alpha$ -Fe corings remain due to the sluggish solid state diffusion.

## Generalized Solidification Model

Numerous models have been proposed to explain the formation of various microstructures in the melt spun alloys, most are concerned with competition between the free energy of nucleation versus growth. These models have a number of shortcomings when

applied to the 2-14-1 system. Two primary deficiencies are the lack of consideration for the peritectic reaction and the failure to account for the effects of the heat released from the crystallization, i.e. recalescence. Recently, model calculations<sup>66</sup> have shown that the length of time spent in a quasistatic state between the liquidus and the solidus is sufficient for the breakup of the dendrites formed in the initial solidification, which results in a fine equiaxed microstructure. Furthermore, this dendritic breakup appears to be dependent on the degree of undercooling, which only occurs when the undercooling has reached a critical value  $\Delta T^*$ . This discovery successfully explains the existence of a critical undercooling separating dendritic and fine equiaxed microstructure observed in many binary alloys<sup>67-68</sup>, and it has recently been extended<sup>69-70</sup> to peritectic materials, where the changes taking place in the temperature and velocity of the solidification front, as well as the temperature gradient at the front, can rapidly alter the solidification process. Since our analysis of melt spun 2-14-1 has also shown some unique features that can not be explained by the conventional models, which include the clear transition from the fine equiaxed to coarsely grained 2-14-1 with  $\alpha$ -Fe dendritic inclusions and the uniformity in size of the equiaxed 2-14-1 grains across ribbons melt spun at 20 m/s, a generalized solidification model modified by the dendritic breakup during recalescence is therefore being proposed. The following discussion will demonstrate how various microstructures can be formed using this generalized model.

In this discussion, we define:  $T$  = the initial undercooled temperature (just before nucleation),  $T_l$  = liquidus temperature,  $T_p$  = peritectic temperature,  $T_n$  = nucleation temperature (homogeneous nucleation  $T_n^{\text{ho}}$  and heterogeneous nucleation  $T_n^{\text{he}}$ ,  $T_n^{\text{he}} > T_n^{\text{ho}}$ ),  $T_g$  = glass transformation temperature,  $T_r$  = maximum recalescence temperature,  $\alpha$  = primary

solidification product, in this case  $\gamma\text{-Fe}$ ,  $\beta$  = peritectic phase,  $\text{Liquid} + \alpha \rightarrow \beta$  at  $T_p$ , in this case  $\text{Nd}_2\text{Fe}_{14}\text{B}$ .

Since no practical phase transformation occurs as in equilibrium situation, and the melt spinning in particular provides far off-equilibrium condition for solidification, undercooling is both necessary and dominant in the formation of various 2-14-1 melt spun microstructures. There are three cases categorized according to the degree of undercooling achieved just before nucleation (represented by the initial undercooled temperature  $T$ ) that need to be considered to fully explain the solidification process of such a peritectic.

(1)  $T_p < T < T_l$

This case is close to the equilibrium situation: the solidification process begins with the primary reaction  $L \rightarrow \alpha$ , upon further cooling  $\alpha$  phase nucleates and grows. Once  $T_p$  has been reached,  $\beta$  phase nucleation takes place from the primarily solidified  $\alpha$  phase through the peritectic reaction  $L + \alpha \rightarrow \beta$ . Growth of the  $\beta$  phase needs to continuously transport iron atoms across the  $\alpha/\beta$  interface and consume the  $\alpha$  phase, resulting in microstructures with  $\alpha$  corings (inclusions) inside  $\beta$  grains.

Therefore, the primary solidification of  $\alpha$  phase brings diversity into the microstructures that may form in this case. Upon cooling,  $\alpha$  phase may nucleate heterogeneously if the initial undercooled temperature is higher than the homogeneous nucleation temperature of  $\alpha$  phase but lower than its heterogeneous nucleation temperature,  $T_n^{\text{ho}}(\alpha) < T < T_n^{\text{he}}(\alpha)$ . These  $\alpha$  nuclei then grow dendritically or columnar along the direction of the temperature gradient and become dendritic (or columnar) inclusions eventually. Because of the positive temperature gradient across the melt spun ribbons,

alignment of these primarily solidified  $\alpha$  dendrites may be achieved and thus so-formed microstructure may be textured. If larger undercoolings have been achieved before the nucleation,  $T_p < T < T_n^{ho}(\alpha)$  for example, copious nucleation of the  $\alpha$  phase is possible based on the compositional fluctuation and impurities, and thus microstructures with spherical (or particular)  $\alpha$  corings may form.

$$(2) T_g < T < T_p$$

Once the quenching is strong enough to hold the melt until  $T_p$  has been reached,  $\beta$  phase becomes thermodynamically more favorable and the primary solidification is inhibited (or suppressed). If  $T_n^{ho}(\beta) < T < T_n^{he}(\beta)$ ,  $\beta$  phase nucleates heterogeneously and grows. The growth front of the  $\beta$  phase can move very rapidly so that the heat of crystallization released exceeds the heat dissipation rate through the solid layer and the interface with the wheel. The temperature of the material, then starts to rise. This is referred as recalescence. The recalescence produces a negative temperature gradient across the solidification front which makes the growth front unstable and favors dendritic growth, and will reach its maximum at temperature  $T_r$ , which is determined by the balance of the specific heat of the liquid, the specific heat of the solid phases, the heat of crystallization of  $\beta$  phase, the volume fraction of the phase formed, the degree of initial undercooling and the heat extraction rate of the wheel. If  $T_r < T_p$ , or even if  $T_r > T_p$  but the time remaining on the quasistatic plateau is not long enough to break the  $\beta$  dendrites ( $\Delta t_r < \Delta t_{bu}$ <sup>66</sup>), columnar  $\beta$  phase will form and remain, as in the microstructures observed in some gas atomized powders<sup>71</sup> and ribbons melt spun on a steel wheel<sup>64</sup>. The case of interest here is  $T_r > T_p$  and  $\Delta t_r > \Delta t_{bu}$ , since the temperature now is above  $T_p$ ,  $\beta$  dendrites that formed initially are unstable and begin to dissolve. Given enough



time, these dendrites will eventually break up into fine segments and act as nucleation sites based on which a fine equiaxed microstructure will later be formed. Meanwhile, nucleation of the  $\alpha$  phase can occur in the interdendritic regions, and this phase can grow into small particles residing in  $\beta$  grain conjunctions. This dendritic breakup model elucidates the cause of many equiaxed microstructures which are generally explained as due to copies homogeneous nucleation and appears potent to explain the experimental facts that can not be explained using conventional models. An example is the clear transition from the fine equiaxed 2-14-1 grains to the very coarse grains with dendritic  $\alpha$ -Fe corings observed in  $\text{Nd}_2\text{Fe}_{14}\text{B}$  @  $10\text{ms}^{-1}$  ribbons. Because fine equiaxed grains are generally assumed in conventional models from copious homogeneous nucleation events, which suggest that the initial undercooled temperature just before the solidification should be lower than  $T_n^{\text{ho}}(\beta)$ , that is  $T < T_n^{\text{ho}}(\beta)$ . Whereas, the presence of the primarily solidified Fe corings across the boundary suggests that the local initial undercooled temperature is higher than  $T_p$  ( $T > T_p$ ). Therefore, a discontinuity in temperature arises inside the ribbons which seems highly unlikely, and invalidates the above explanation. Based on our model, the presence of the clear transution is actually because the growth of the initial 2-14-1 dendrites is stopped by the nucleation and dendritic growth of the primary Fe phase where  $T_p < T < T_l$ . Furthermore, as analyzed earlier, the sinusoid-like curved boundary between the optically fine and coarse grains along the under-quenched ribbons suggests that the solidification of these ribbons begins with heterogenous nucleation of the 2-14-1 phase from the liquid on the wheel surface and grows dendritically along the temperature gradient. The only reason that fine equiaxed instead of columnar 2-14-1 grained microstructure has been formed is the breakup of the original 2-14-1 dendrites

during the recalescence.

If the melt is suppressed nucleation to enough low temperatures such as  $T_g < T < T_n^{ho}(\beta)$ ,  $\beta$  phase can readily nucleate from internal compositional fluctuation or impurity instead of from outside substrate, equiaxed or spherical 2-14-1 microstructure may form from so-called homogeneous nucleation, as occurs in the devitrification of over-quenched 2-14-1 glass. The difference for quenched ribbons is however, the existence of a positive temperature gradient across the ribbon thickness and thus a change in grain size from one side to the other, since grain size in such rapid quenching is generally “nucleation controlled” and higher degree of undercooling results in more homogenous nucleation events.

### (3) $T < T_g$

Glass begins to form wherever  $T < T_g$ , and the lower the temperature that the melt has been suppressed nucleation, the more stable the glass that has formed.

## **Solidification Process in the Melt Spun 2-14-1 Alloys**

The solidification process in the melt spinning of 2-14-1 alloys can thus be explained using the above categorized solidification model. The explanation will begin with a discussion about the heat transfer occurring during the melt spinning process. One face of a ribbon is brought at time  $t = 0$  into contact with a heat sink of the wheel which is at a lower uniform temperature of  $T_w$ . It is assumed that a thin film is formed instantly at the melt/wheel interface, though which the melt is cooled by 1-D heat flow in the  $x$  direction from the free side and normal to the interface at  $x = R$ . Therefore, the heat transfer is determined jointly by the melt and the film, among which the poorer one is the bottleneck and the controlling

factor. Conduction is considered as the dominant term for simplicity, and the rate of heat flow per unit of area ( $q$ ) inside the melt is given by Fourier's law:

$$q = -k \frac{\partial T}{\partial x}$$

where  $k$  is the bulk thermal conductivity and  $x$  is defined as the distance away from the free side. The heat transfer through the film is described by Newton's law of cooling, and  $q$  is given by:

$$q = h(T_R - T_w)$$

where  $h$  is the film heat transfer coefficient and  $T_R$  is the melt temperature adjacent to the film at  $x = R$ . The heat transfer rate obtained from the melt and the film must be equal to ensure continuous heat flow, and from which the slope of the temperature ( $G$ ) inside the melt is given by:

$$G = \frac{\partial T}{\partial (-x)} = \frac{h}{k}(T_R - T_w)$$

Since during the melt spinning,  $T_R$  is much higher than  $T_w$  (tens or several hundreds degrees higher) and  $h$  is dependent on the wheel speed ( $v$ ) and has been reported to be  $10^4 \text{ W.m}^{-2}.\text{K}^{-1}$  and above<sup>61</sup>,  $G$  is usually positive and a positive gradient is generally assumed across the ribbon thickness. The temperature gradient  $G$  changes however with the wheel speed, and the slope change can be obtained by taking the first derivative of the  $G$ :

$$\frac{\partial G}{\partial v} = \frac{1}{k} \left[ \frac{\partial h}{\partial v} (T_R - T_w) + h \frac{\partial T_R}{\partial v} \right]$$

In the vicinity of solidification,  $h$  increases linearly with the increase in  $v$ , but  $T_R$  decreases almost linearly with the speed's increase<sup>61</sup>, thus it is not a easy task to predict the

change of the temperature slope. Fortunately, because  $h$  is usually two order of magnitude higher than  $(T_R - T_w)$  which gives  $\frac{\partial T_R}{\partial v}$  a bigger weighing factor, the slope presumably decreases with the increase in wheel speed. Based on the above discussion, the initial undercooled temperature profile across a ribbon during the melt spinning is qualitatively described as in Figure 13. The curves in the figure represent the temperature profiles at the onset of initial nucleation across the ribbons melt spun at different wheel speeds, and the wheel side temperature ( $T_R$ ) and slope of each curve are two important factors determining the phases that will form and the homogeneity of the overall microstructure. Also as noticed the ribbon thickness is decreasing with the increase in wheel speeds. At 10 m/s, fairly thick ribbons are produced and the difference in the initial undercooled temperature  $T$  across a ribbon is large, as depicted in the Figure 13. Therefore, the solidification begins from the wheel side at  $T_R < T_p$ , precisely  $T_p^{ho} < T_R < T_p^{he}$ , and thus heterogeneous nucleation of the 2-14-1 phase occurs at the wheel surface which grows dendritically across the ribbon, this is one growth front. Meanwhile, there is another growth front of free iron phase due to the fact that the temperature profile has an intersection with the peritectic temperature  $T_p$ , which means, somewhere inside the ribbon,  $T$  is higher than  $T_p$  and the primary solidification of the free iron phase is preferred, which grows dendritically (or columnar) toward the free surface. Recalescence occurs with the nucleation and growth of both two phases, and raised the local temperature. According to the microstructure formed at this wheel speed, the recalescence has raised temperature of the first region to  $T_r > T_p$  and stayed long enough to break the 2-14-1 dendrites, and fine equiaxed 2-14-1 grains later form on these dendritic segments during cooling below  $T_p$ , also during the recalescence secondary free iron phase

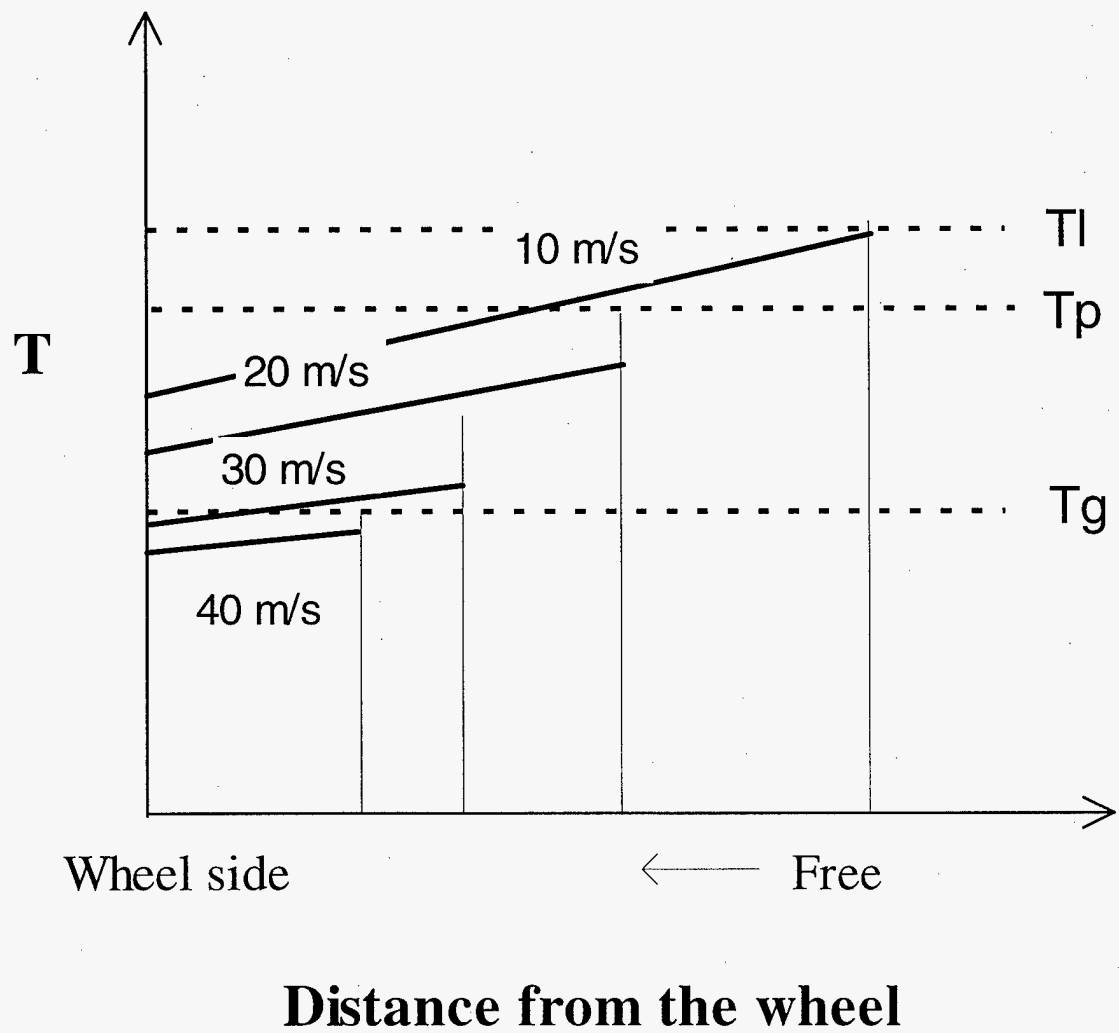


Figure 13 Schematic temperature profile across a ribbon at the onset of nucleation

forms and resides at grain conjunctions. On the other hand, the region beginning with free iron phase has developed coarse 2-14-1 grains with free iron dendritic inclusions, and these grains are textured with the c-axis normal to the ribbon surface.

With the increase in wheel speeds, both the wheel side temperature and the slope of the temperature profile at the onset of the nucleation decrease. For ribbons melt spun at 20 m/s, a through quenching has been achieved which results in fine equiaxed 2-14-1 grains and homogeneity of the microstructure, as shown in those SEM and TEM images. Most of each ribbon has been undercooled to  $T < T_p$  before the occurrence of nucleation, though a thermal gradient still exists across the ribbon thickness, only one growth front of the 2-14-1 phase exists. Heterogeneous 2-14-1 nucleation begins from the wheel surface and grows dendritically through the whole ribbon. These dendrites break up during recalescence and a uniform equiaxed microstructure is formed just as described before. One thing worth of mention is that the breaking up of 2-14-1 dendrites during the recalescence is always accompanied by the formation of the secondary free iron phase ( $T_r > T_p$ ), which grows into fine particles residing in the conjunctions of 2-14-1 grains, and thus few percent of free iron is present in the optimally-quenched 2-14-1 microstructure. The 30 m/s wheel speed suppresses the wheel side temperature  $T_R$  below the glass forming temperature  $T_g$ , and substantial amount of glassy 2-14-1 forms adjacent to the wheel side. However, there is a region close to the free side where  $T_p > T > T_g$ , precisely  $T_n^{ho} > T > T_g$ , where homogeneous nucleation of the 2-14-1 phase occurs, and because of rapid heat extraction rate at this high wheel speed, temperature cools down below  $T_g$  before this region is fully crystallized and some glass remains at intergranular regions, as shown in the TEM image of the crystallized

region from a  $\text{Nd}_2\text{Fe}_{14}\text{B}$  @  $30\text{ms}^{-1}$  ribbon flake. Similar microstructure can also be found in the annealed samples from the over-quenched glassy precursor.

When the wheel speed reaches 40 m/s, almost all parts of each ribbon have been undercooled to  $T < T_g$  and featureless glassy matrix is formed throughout the whole ribbon. Some 2-14-1 nuclei however may be present due to possible temperature fluctuation which causes the temperature of some regions higher than  $T_g$  and thus 2-14-1 phase begins to nucleates there. These nuclei may be quenched to the room temperature if they have not enough time to grow, and two of these 2-14-1 nuclei have been shown in Figure 12 . Meanwhile, the amorphous 2-14-1 formed in 40 m/s ribbons is more viscous than that formed at 30m/s because of larger degree of undercooling achieved.

### **C-axis Texturing**

As a constraint for solidification models, the phenomenon of c-axis texturing was observed in melt spun ribbons and will be fully analyzed. The existence of the c-axis texturing in quenched 2-14-1 ribbons is a result of combining a peritectic to the melt spinning process, a special application of our generalized solidification model.

The c-axis texturing was first observed in 2-14-1 ribbons melt spun at 10 m/s. Figure 14 shows XRD results of ribbon and powdered samples made from these ribbons. As noted, there is an enhancement in intensity of the 2-14-1 (001) reflections normal to the ribbon surface compared to those for random orientation, which are about 9 %, 25 % and 7 % of the (410) intensity for (004), (006) and (008) reflections respectively, and this enhancement is more pronounced on the free side compared to the wheel side.

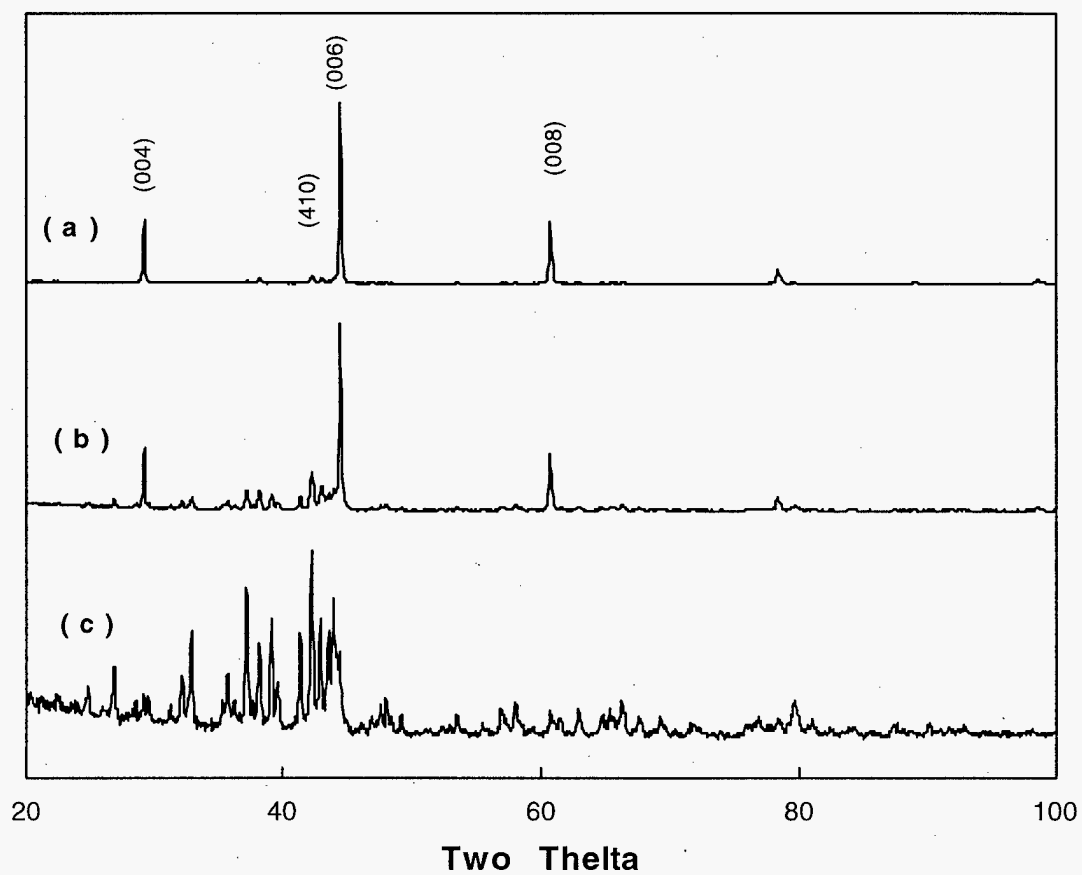


Figure 14 Cu K $\alpha$  X-ray diffraction patterns of Nd<sub>2</sub>Fe<sub>14</sub>B@10 ms<sup>-1</sup> ribbon flakes:  
(a) free side; (b) wheel side; (c) powdered samples



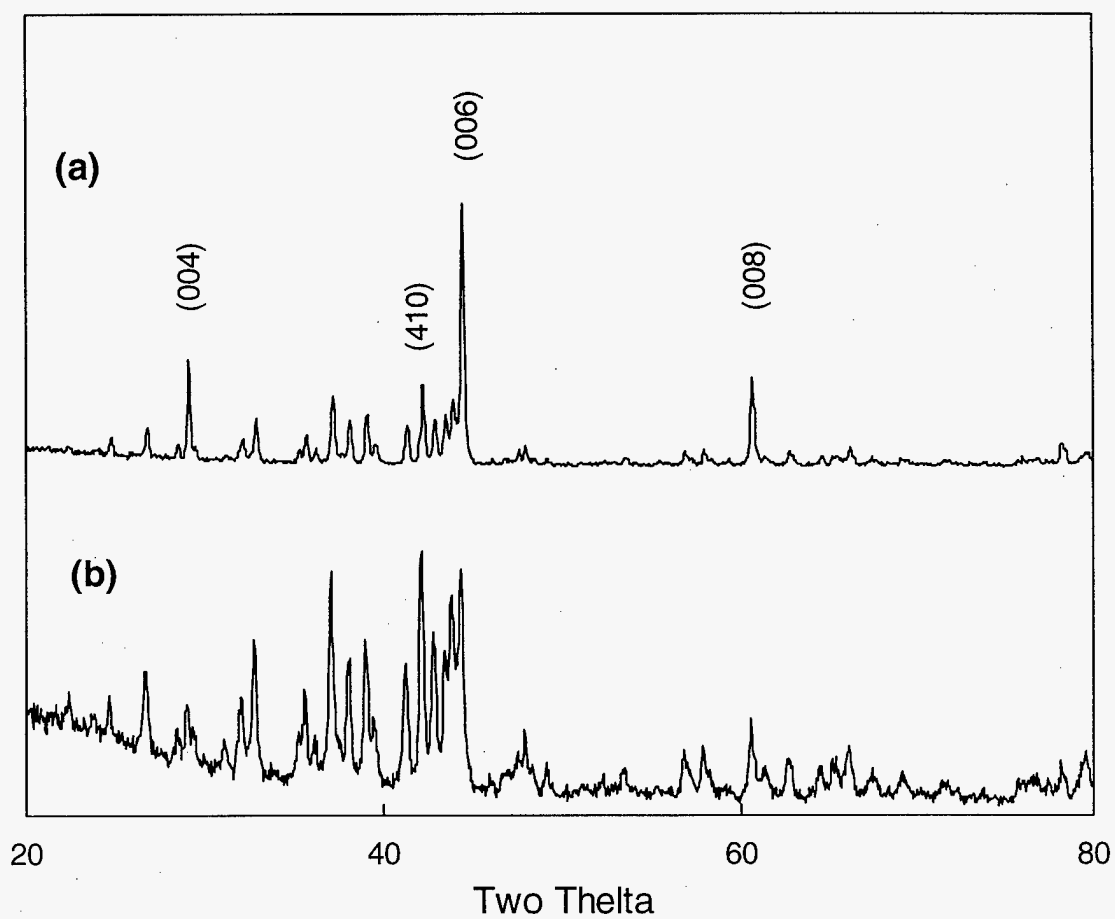


Figure 15 Cu K $\alpha$  X-ray diffraction patterns of Nd<sub>2</sub>Fe<sub>14</sub>B@17ms<sup>-1</sup> ribbon flakes:  
(a) free side; (b) wheel side

It has been known from the microscopic study on these ribbons that they are composed of equiaxed 2-14-1 grains with varying size cross the thickness and a sinusoid-like curved boundary separates the coarse grains and the fine ones (in Figure 7). It has also been shown from calculations that 10 % of Cu K $\alpha$  X-ray ( $\lambda = 0.1542$  nm) can penetrate Nd<sub>2</sub>Fe<sub>14</sub>B as deep as 13.2  $\mu$ m and 17.6  $\mu$ m for  $2\theta = 44.3^\circ$  and  $60.7^\circ$  respectively, which suggests that the structural information such as the (00l) reflections can be collected from a region  $> 10$   $\mu$ m below the ribbon surface. Therefore, the coarsely grained regions representative of the free microstructure shown in Figure 5d is believed to be textured with the c-axis of the 2-14-1 phase normal to the ribbon surface, and the only reason for the texturing observed from the wheel side ribbon samples is because of the penetration of this textured microstructure through thickness along these ribbons and also the X-ray. This is further confirmed by the XRD result conducted on ribbons melt spun at 17 m/s, as shown in Figure 15, the similar enhancement is present on the free side but absent from the wheel side, because more effective quenching has been achieved which pushes the curved interface completely away from the wheel side beyond the X-ray penetration depth.

The XRD results for stoichiometric 2-14-1 ribbon samples (in Figure 16) show that the c-axis alignment on the free side decreases with the increase in wheel speeds from 10 to 17 m/s, and disappears at 20 m/s. This decrease coincides with the decrease of the  $\alpha$ -Fe phase fractions as determined by VSM, which are 3.91%, 3.49%, 3.15% and 2.50% for 10, 15, 17 and 20 respectively. In addition, the disappearance of the c-axis alignment at 20 m/s marks the transition from the under-quenched condition to the optimally-quenched condition, which implies the disappearance of the coarsely grained free side microstructure. All these seem to

suggest a correlation between the c-axis texturing and the primarily solidified Fe phase, also keep in mind that the free iron phase experimentally measured includes both the primary Fe phase and the secondary one which, as explained in the model, forms accompanying to the breakup of the 2-14-1 dendrites during the recalescence. Furthermore, a specific quenching region seems essential for the texturing formation in such a way to provide directional solidification across the ribbon thickness and to grow the primary iron phase prior to the nucleation of the 2-14-1 phase.

In fact, texturing phenomenon in 2-14-1 melt spun ribbon flakes have been observed and studied by several research groups<sup>23,72-74</sup>. The fact that this c-axis texture arises from equiaxed 2-14-1 grains puzzled them and also defies the conventional explanation of growth selection of favorably oriented crystallites, since the preferred growth direction of the tetragonal 2-14-1 has been reported<sup>75</sup> to be along the 'a' axis in the basal plane instead of the 'c' axis.

The key to this puzzle has been found in the TEM study on the free side microstructure of the  $\text{Nd}_2\text{Fe}_{14}\text{B}@10\text{ms}^{-1}$  ribbon flakes. TEM samples made as planar section polished preferentially from the wheel side of the ribbons reveal that Fe inclusions have elliptical cross section with some approaching nearly spherical dimensions yet nearly all of the inclusions have identical orientation within a single 2-14-1 grain, as shown in Figure 17. Furthermore, there appears to be an epitaxy between these Fe inclusions and the host 2-14-1 grain with  $(110)_{\alpha\text{-Fe}}// (330)_{2-14-1}$  and  $[1-11]_{\alpha\text{-Fe}}// [001]_{2-14-1}$  as indicated by the SADP and CEBD shown in the inserts.

A possible conclusion deduced from the above observations is that the Fe inclusions

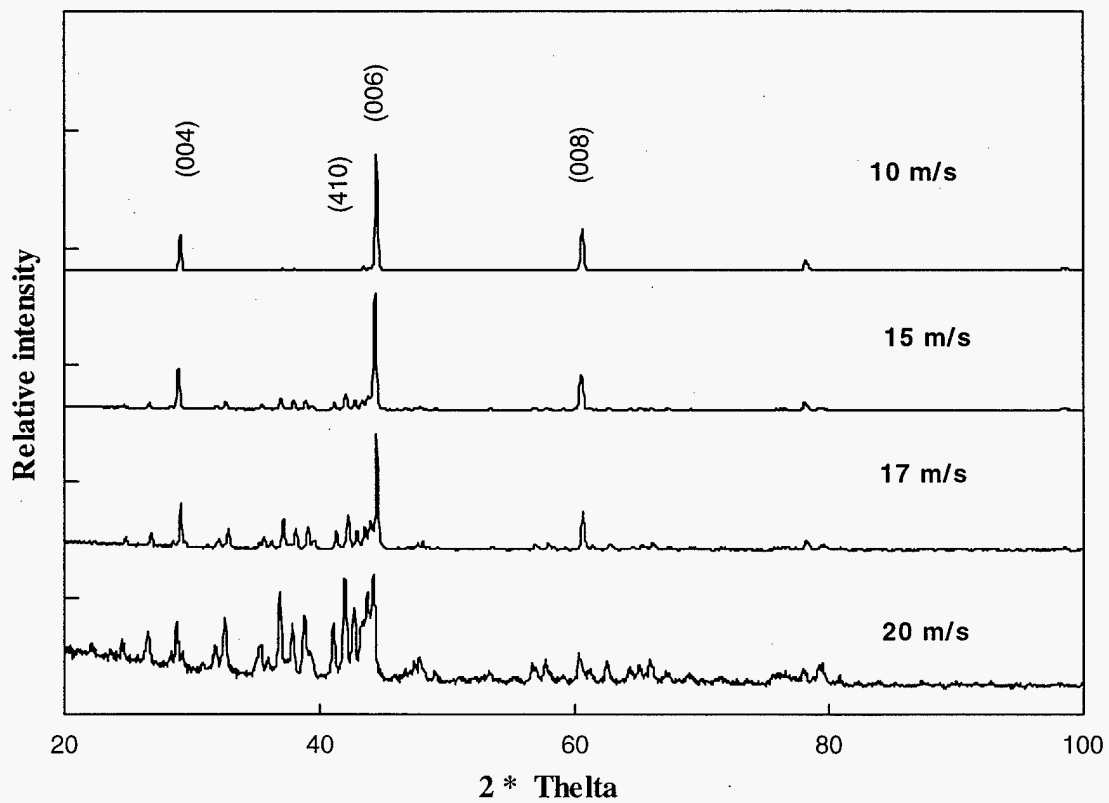


Figure 16 XRD results on free sides of stoichiometric 2-14-1 ribbons

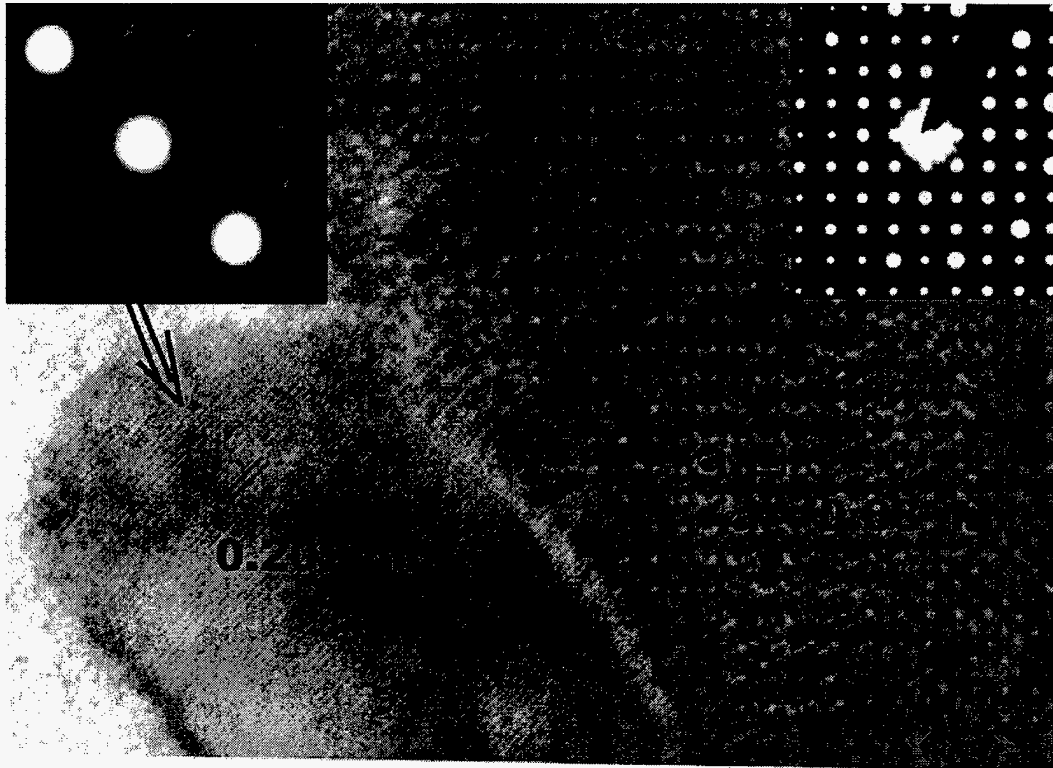


Figure 17 TEM image from planer surface of a Nd<sub>2</sub>Fe<sub>14</sub>B @10ms<sup>-1</sup> ribbon ,  
SADP of the matrix and CBED from the Fe inclusion inserted

are a result of formation of Fe dendrites during the primary solidification at a temperature above the peritectic temperature ( $T_p$ ) when under-quenched. At low wheel speeds, heat extraction rate is relatively low and can not suppress nucleation from all of the alloys to below  $T_p$ . As presented in our model, Fe dendrites can grow dendritically in the direction of the thermal gradient where  $T_p < T < T_l$ . As the temperature cools back below  $T_p$ , the remaining liquid in this region reacts with the aligned Fe dendrites to induce the (001) texture in melt spun 2-14-1 alloys. The identification of the growth direction of the Fe dendrites is complicated by the  $\gamma$  to  $\alpha$ -Fe transformation, and it is assumed that the dendrites form as  $\gamma$ -Fe dendrites with the primary growth direction of  $\langle 110 \rangle$ , which is the most closely packed direction in FCC structure. It should be kept in mind that the growth direction of dendrites with cubic crystal structure is generally considered as  $\langle 001 \rangle$  direction, which is the axis of a pyramid sided with the most closely packed planes and resulted from competition and compromise of the fast growth directions, such as the  $\langle 110 \rangle$  direction for FCC crystal structure. The situation may have however changed in the dendritic growth of the primary Fe phase during the melt spinning because only a small amount of the Fe phase can form from the stoichiometric composition, that is, the so-formed Fe dendrites are surrounded by large volume of liquid and thus sparsely distributed Fe nuclei can grow without competition, and only dendrites with fast growth directions along the temperature gradient grow fast and remain.

Upon cooling, the 2-14-1 phase will nucleate at the  $\gamma$ -Fe/melt interface because a epitaxy exists between the  $\gamma$ -Fe and the 2-14-1 with  $(111)_{\gamma\text{-Fe}} // (330)_{2\text{-}14\text{-}1}$ , which lowers the surface energy. Because of the preferred nucleation sites, the original Fe dendrites become

enveloped and eventually included in the 2-14-1 grains. Since the preferred growth direction of  $\gamma$ -Fe is  $\langle 110 \rangle$ , the so-formed 2-14-1 grains align with their [001] direction perpendicular to the ribbon surface, and this would explain the apparent epitaxy between Fe and 2-14-1. Direct determination of the original epitaxy is however difficult to conduct due to the  $\gamma$  to  $\alpha$ -Fe transformation upon further cooling.

The initial composition and the melt spinning parameters including the superheat (the shooting temperature), the size of the crucible orifice, the over-pressure and the wheel speed all affect the (001) texturing, since they all contribute to the initial undercooled temperature ( $T$ ) across the ribbons and the direction of the temperature gradient. The texture has been formed for all the compositions ranging from Fe-rich to Nd-rich, as shown in Figure 18. The degree of the (001) alignment, measured as an intensity ratio of the (008) and (410) reflections ( $I_{008}/I_{410}$ ), is wheel speed dependent. It is however not a simple monotonic decay with the increase in wheel speeds as reported by some research groups<sup>23</sup>, a maximum is present instead for each composition tested at a wheel speed about 10 m/s--the optimum wheel speed for the texture, as noted in the Figure 18. The existence of this optimum speed can be explained using our model previously presented, which is determined by optimizing the amount of the Fe dendrites formed during the primary solidification and the degree of their alignment. At the optimum wheel speed, an excellent combination of just right amount of Fe phase and a perpendicular temperature gradient has been achieved. Further increase of the wheel speed, though ensures the perpendicular temperature gradient across the ribbon thickness, pushes both the region of the coarsely grained free side microstructure and the sinusoid-like curved boundary out of the ribbons, which disappear with the c-axis alignment

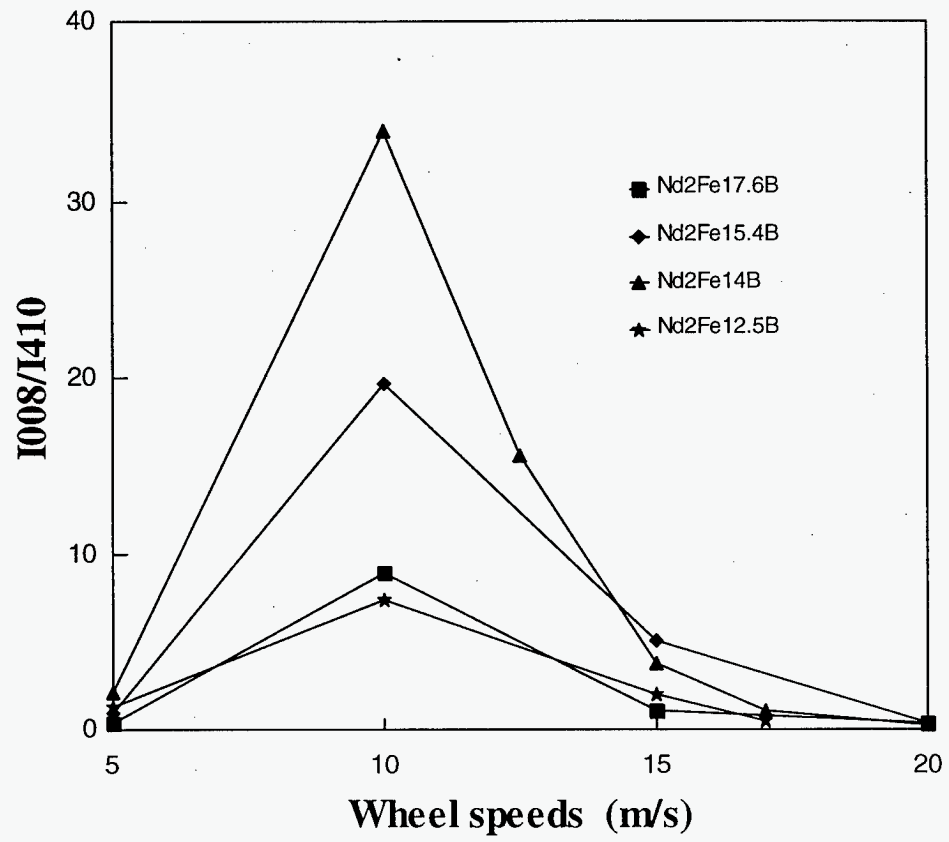


Figure 18 Degree of (001) texture vs. wheel speeds at different compositions



when the wheel speed reaches 20 m/s. Lower wheel speeds, 5 m/s for example, can produce more phase fraction of the primarily solidified Fe phase and extend the region of the coarsely grained microstructure, two factors however deteriorate the c-axis alignment, one is the occurrence of secondary branching which disturbs the alignment of the Fe dendrites because the nucleation of 2-14-1 phase can now take place from the secondary arms instead of originally just the primary arms, as can be seen from the planar TEM image of an under-quenched Fe rich ribbon sample in Figure 19, noticing the less degree of the c-axis texturing from the free sides and secondary branching of the Fe dendrites, and the stress concentration (in Figure 19c) around these Fe dendrites may be attributed to the volume change from the  $\gamma$  to  $\alpha$ -Fe transformation; the second is the change of temperature gradient direction with the wheel speed, though this is not completely understood so far, it is proposed that the temperature gradient is not completely perpendicular to the ribbon surface along ribbons melt spun at low wheel speeds, some regions inside these ribbon, the direction of the temperature gradient is away from the perpendicular direction and takes an angular distribution. Therefore, the primarily solidified Fe dendrites can now grow in scattered directions and only part of them are aligned perpendicular to the ribbon surface. If this is true, the angular temperature gradient distribution in regions close to the free side may be studied by measuring the angular distribution of the (001) texturing on the free surface of the ribbons. In addition, stoichiometric 2-14-1 has shown the highest degree of the alignment in the tested composition range.

Shooting temperatures (overheats) also have some effects on the formation of the c-axis texturing because they affect the effective quenching (initial undercooled temperature  $T$ )

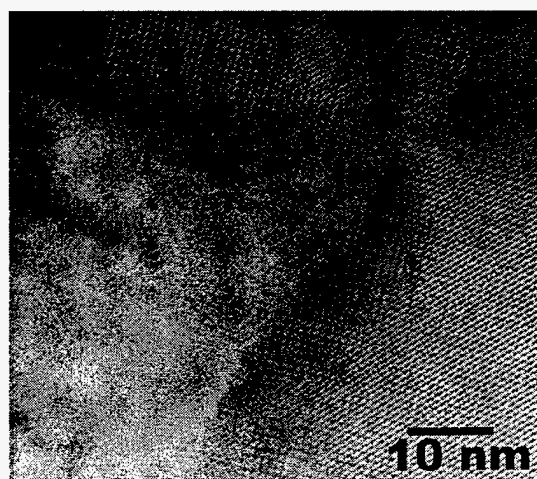
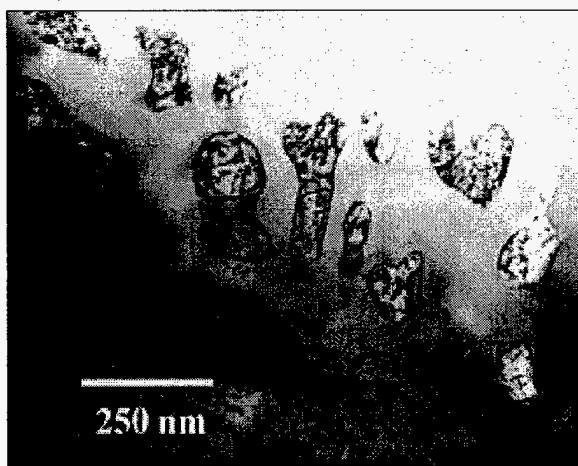
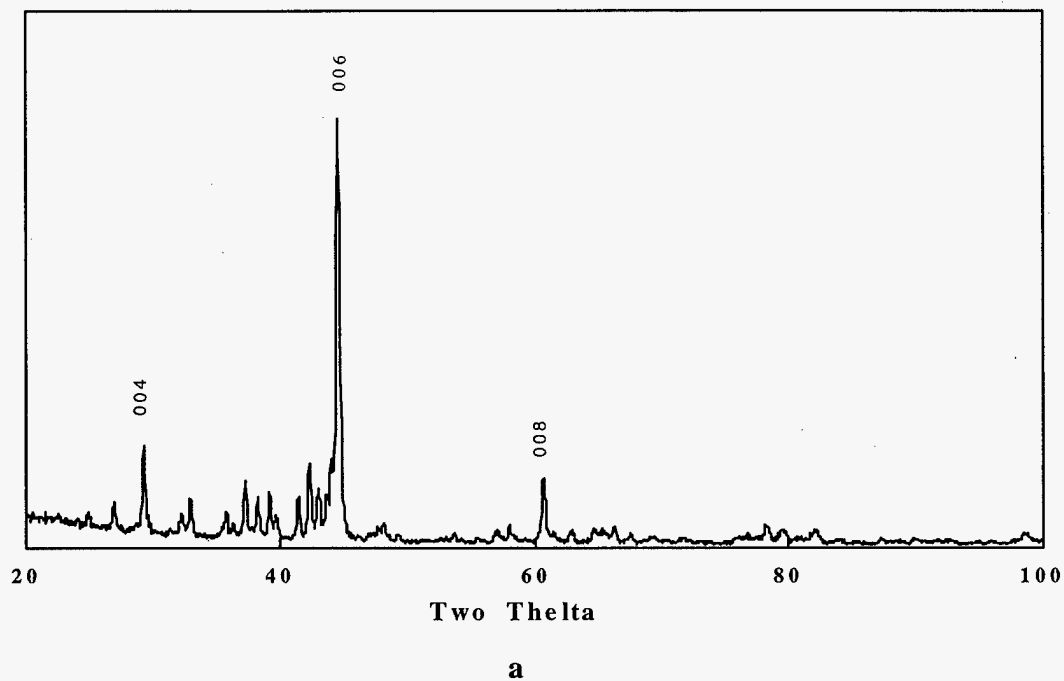


Figure 19 Results from under-quenched Fe rich ribbon flakes:

- a. Cu K $\alpha$  X-ray diffraction pattern of the free sides;
- b. TEM image of the free side surface showing dendritic Fe;
- c. showing the stress around the Fe inclusions TEM image

achieved during the melt spinning. It is generally believed that higher shooting temperatures mean less effective quenching, and it makes sense that the optimum wheel speed for the texturing is increased from 10 m/s to 12.5 m/s when increasing the shooting temperature from 1375°C to 1450°C, as shown in Figure 20. In addition, the degree of the (001) texture at a specific wheel speed above the optimum can be used qualitatively to measure the relative quenchability, the higher degree of the texture, the lower quenchability. An example can be found by checking the degree of the texture at 20 m/s when melt spun from different shooting temperatures, the intensity ratio of (008) and (410) reflections is 2.19 for ribbons melt spun from 1450°C but only 0.30 (not appreciable) for the 1375°C quenching, which is consistent with their quenchability.

This principle can be applied to measure the quenchability when using different melt spinning wheels. As we have known that the quenchability decreases as we changing wheel material from Cu to Al to Fe due to the decrease in the thermal conductivity, and this has been confirmed by measuring the degree of amorphization with wheel speeds on 6 at. % TiC added 2-14-1 alloys. The degree of the C-axis alignment at 20 m/s can also be used as a comparison of quenchability between different wheels being used, and the XRD result is shown in Figure 21, the  $I_{008}/I_{410}$  ratio is calculated as 0.30, 0.62 and 2.27 for Cu, Al, and Fe wheel respectively, which yield a consistent result with the amorphization experiment.

The c-axis texturing is very important in the development of magnetic properties, especially the remanence. Though excellent magnetic properties have been produced in textured samples made from hot deformation or HDDR process, the texturing in quenched samples has not been successfully used due to its association with the primary solidification

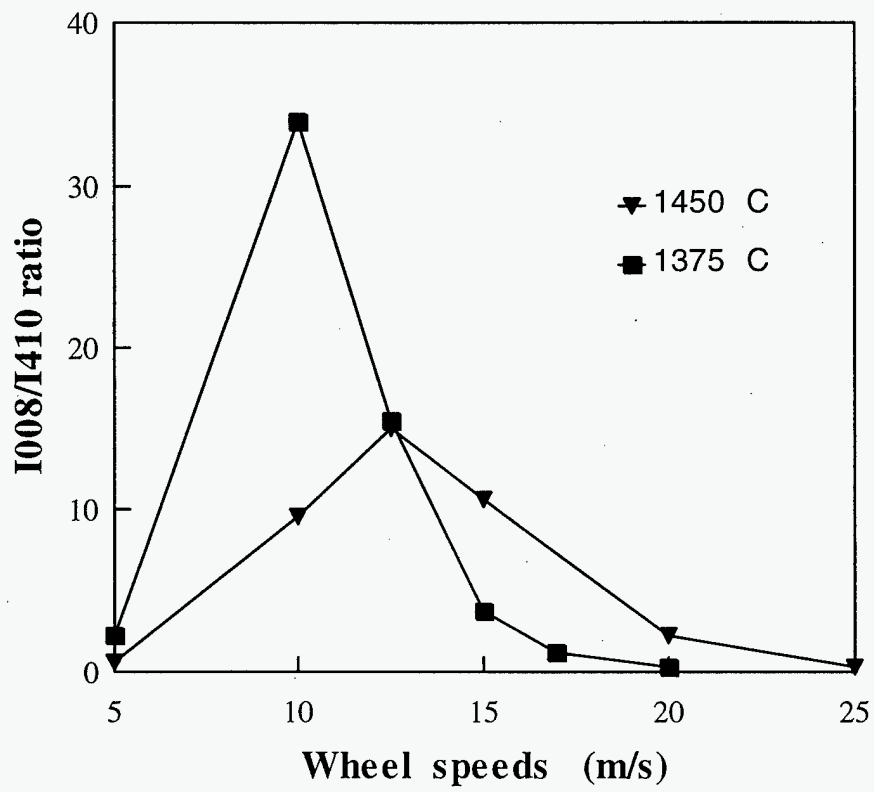


Figure 20 The degree of (001) texture vs. wheel speeds at different shooting temperatures

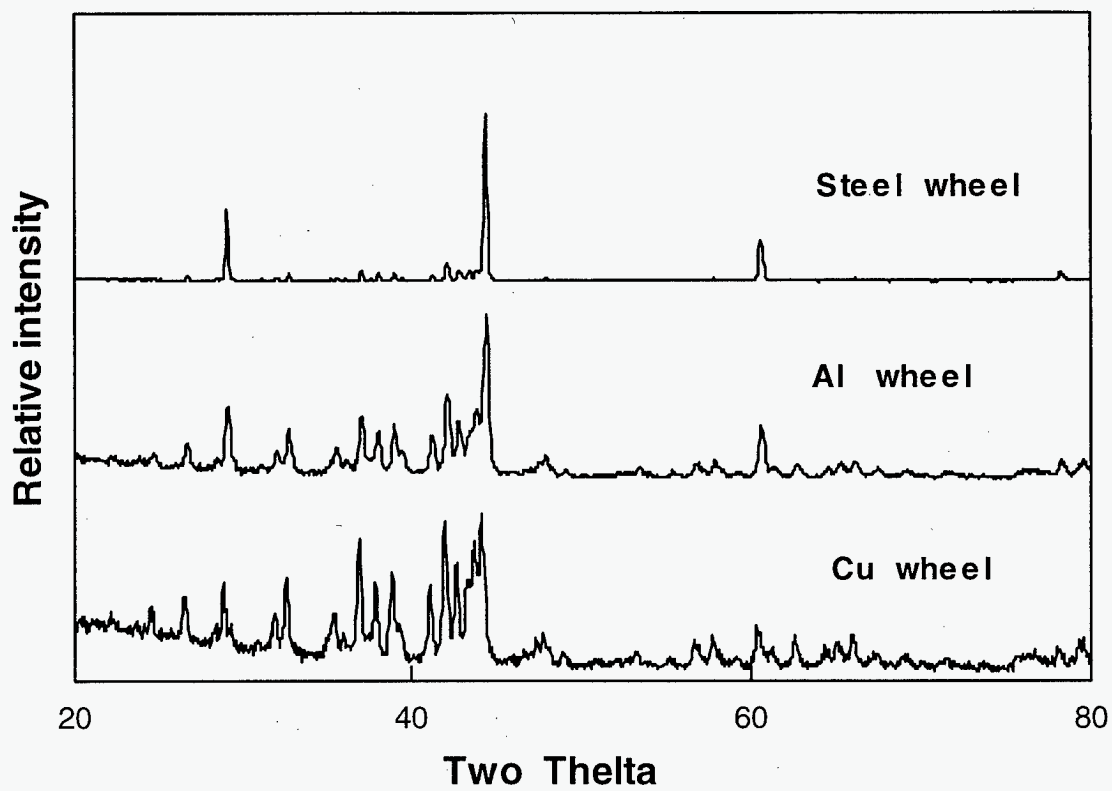


Figure 21 XRD results on free sides of melt spun 2-14-1 @ 20 m/s using different wheels.

and the formation of the coarsely grained microstructure (on the order of microns), since single domain particles ( $< 300$  nm) are generally considered ideal and necessary to develop high coercivity. However, the texturing does have effects on the magnetic properties of the quenched ribbons, although the measurement of this effect is complicated by the grain size effect and sample size effect (the demagnetizing field). Figure 22 shows the change of remanence and maximum energy product of quenched 2-14-1 ribbons measured with the magnetic field along the ribbons and on powdered samples versus wheel speeds.

The results however must be interpreted by considering the demagnetizing effect, if the demagnetizing factor for ribbon samples is assumed as a value close to 0, then the value is about 0.33 when considering the powders with a size  $< 50$   $\mu\text{m}$  as near spherical, therefore, the magnetic properties measured from the ribbon samples should be significantly larger than their powdered counterparts if no other effect comes into play. As shown in the figure, this holds true for the ribbons melt spun at 20 m/s, however, with the decrease in the wheel speed from 20 m/s, the gap of the magnetic properties between ribbon and the powdered samples is getting smaller. This is because the formation of the c-axis texturing normal to the ribbon surface and thus also normal to the applied magnetic field deteriorates the measured magnetic properties, and the better the alignment, the worse the magnetic properties so measured. The disappearance of this gap between the wheel speed 10 m/s to 15 m/s may mark the point where the deterioration of the magnetic properties due to the c-axis alignment compensates the demagnetizing effect, and at 10 m/s, the properties from the powdered samples become better due to the overwhelming effect from the stronger texture. One thing worthy of mention is the texture formation when 2 at. % TiC is added. By checking the wheel speed 5, 7.5, 10

m/s, no texture has been formed, as can be seen from the XRD results in Figure 23. The reason seems more related to the kinetics than the thermodynamics, since primary solidified Fe phase has been detected in all these ribbons. It is assumed that the accumulation (or segregation) of Ti and C atoms at the growth front not only slows down the growth of the 2-14-1 phase but also the primarily solidified Fe phase, which inhibits its dendritic growth and also the alignment. Meanwhile, the segregation of the Ti and C atoms may provide copious heterogeneous nucleation sites for the primary Fe phase. Therefore, no alignment of the primary Fe phase can form and neither can the 2-14-1 grains. TEM study on 2 at. % TiC added ribbons melt spun at 10 m/s (in Figure 25) is consistent with this assumption, the Fe inclusions observed appear elliptical in both the cross-sectional and the planar views, suggesting their spherical or particular nature of morphology.

### **TiC Modified 2-14-1 Solidification**

Since Nd-Fe-B type magnets are practically made from alloyed compositions, it may be useful to extend our understanding of the solidification process of the melt spun 2-14-1 alloys to some modified microstructures, such as the one modified by TiC addition.

TiC addition even if just a small amount (in particular 2 at.% in this project unless specified) can substantially change the solidification process and the melt spun microstructure. Generally speaking, the TiC modified microstructures are considerably finer and more uniform when under or optimally quenched, and composed of more phase fraction and more stable 2-14-1 glass when over-quenched, compared to their stoichiometric 2-14-1 counterparts. TiC added ribbons melt spun at 10m/s consist of equiaxed 2-14-1 grains with

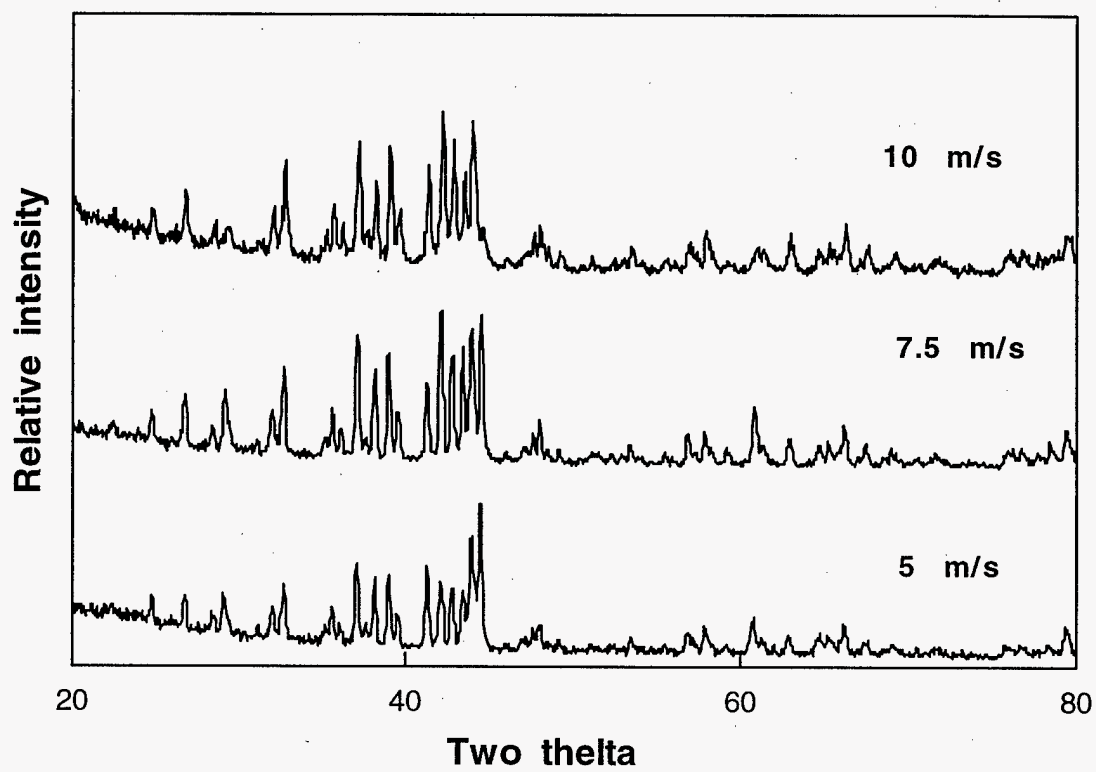
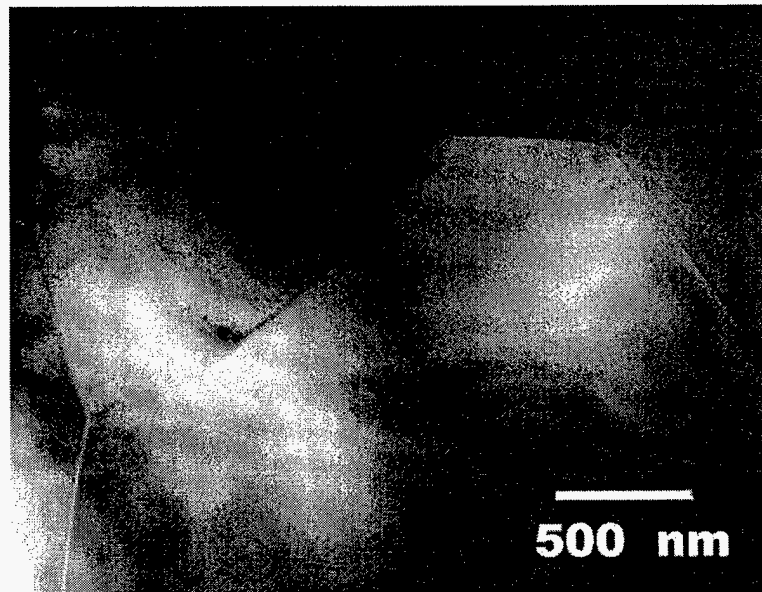


Figure 23 XRD results on free side samples of 2 at.% TiC added melt spun 2-14-1 alloys

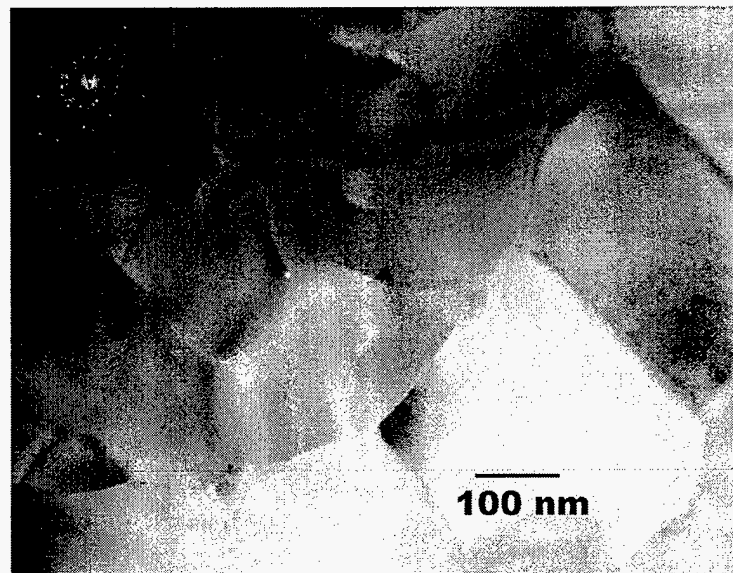


the size changing from a few hundreds nanometers when close to the wheel side to 2-10  $\mu\text{m}$  near the free side, as shown in Figure 24. The similar sinusoid-like curved boundary was also optically observed along the etched ribbon samples, just as their stoichiometric counterpart, except that the boundary seems to be pushed a little away from the wheel side. Although  $\alpha$ -Fe inclusions were also observed and identified in the coarse grains adjacent to the free side, they appear to be spherical instead of dendritic, as can be seen from the cross-sectional TEM image in Figure 25. Meanwhile, although an epitaxy seems present between these spherical  $\alpha$ -Fe inclusions and their host 2-14-1 grain, no texturing has been observed from XRD on the free side of these ribbon samples. Possible explanation may be either because the addition of Ti and C has changed the solidification process in such a way that it reduces the slope and the free side temperature at the onset of nucleation and  $T_p < T < T_n^{\text{ho}}$  ( $\gamma$ -Fe) is achieved in the region close to the free side and the solidification begins there with homogeneous nucleation of free iron phase which is later consumed and encapsulated inside 2-14-1 grains, or kinetically the accumulation of Ti, C at the growth front inhibits the dendritic growth of the free iron phase nucleated heterogeneously and if this is true, Ti and C may be rich around the  $\alpha$ -Fe inclusions.

At 20 m/s, uniform equiaxed microstructure is formed from the wheel side to the free side with the 2-14-1 grain size of 20-30 nm, as shown in the cross sectional TEM images in Figure 26. In addition, substantial amount of amorphous phase has been detected in the DTA, and this microstructure has stepped into the over-quenched region. With the further increase in wheel speed, glassy phase fraction is increasing, and total amorphization is achieved when the wheel speed reaches about 30 m/s.

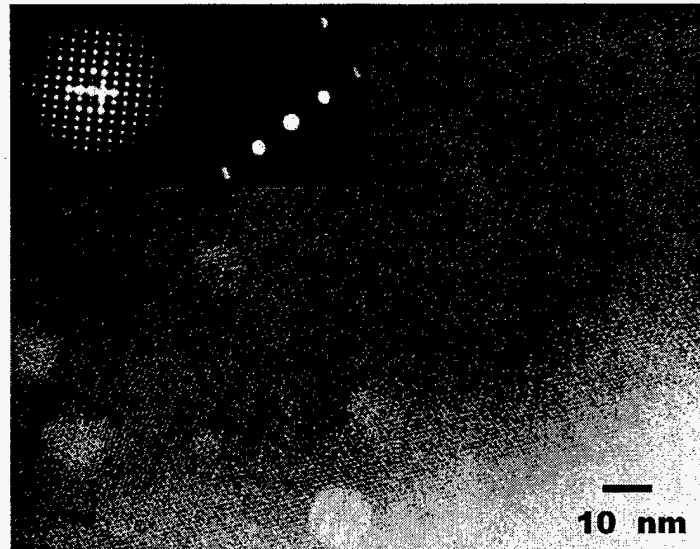


(a)

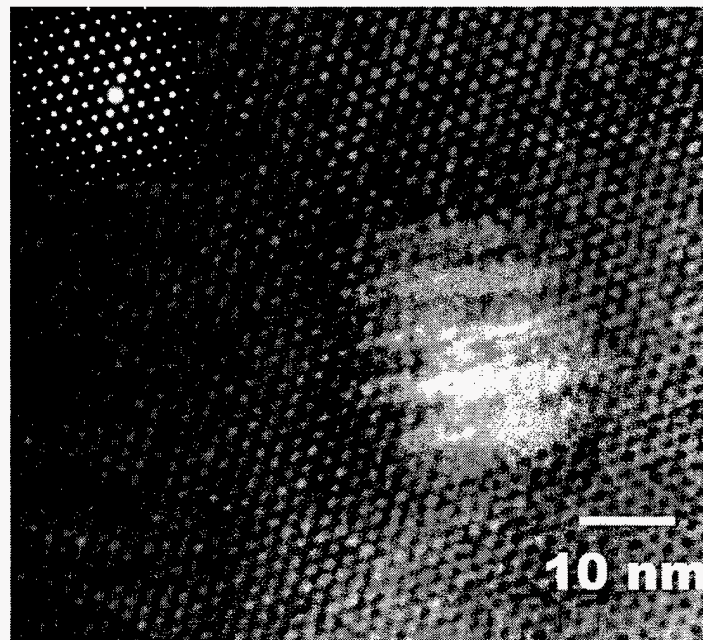


(b)

Figure 24 Cross sectional TEM images of a  $\text{Nd}_2\text{Fe}_{14}\text{B} + 2 \text{ at.}\% \text{ TiC}$  ribbon melt spun at 10 m/s : (a) free side, (b) wheel side



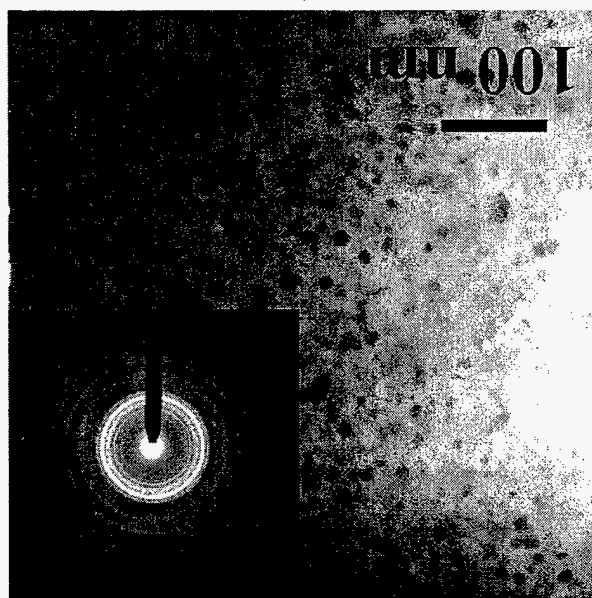
(a)



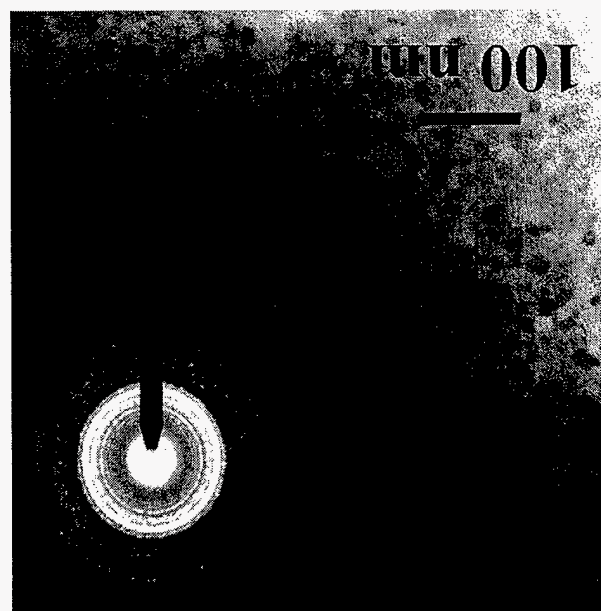
(b)

Figure 25 A cross sectional TEM image of a Nd<sub>2</sub>Fe<sub>14</sub>B + 2 at% TiC ribbon melt spun at 10 m/s showing Fe particles: (a) [0-11] zone , (b) [100] zone.

Figure 26 Cross sectional TEM images from a  $\text{Nd}_2\text{Fe}_{14}\text{B}+2\text{at.\%TiC}$  at  $20\text{ms}^{-1}$  ribbon: (a) free side , (b) wheel side.



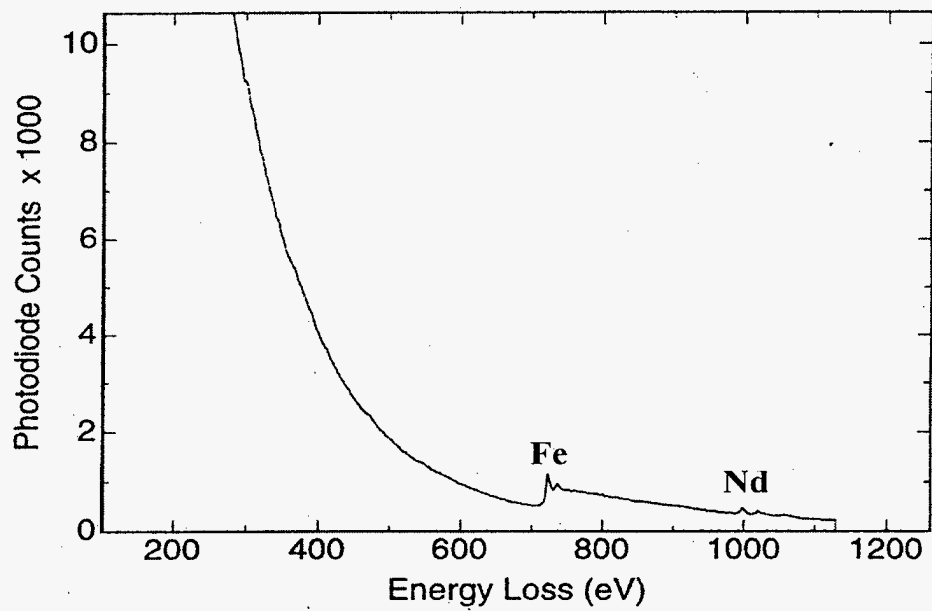
(b)



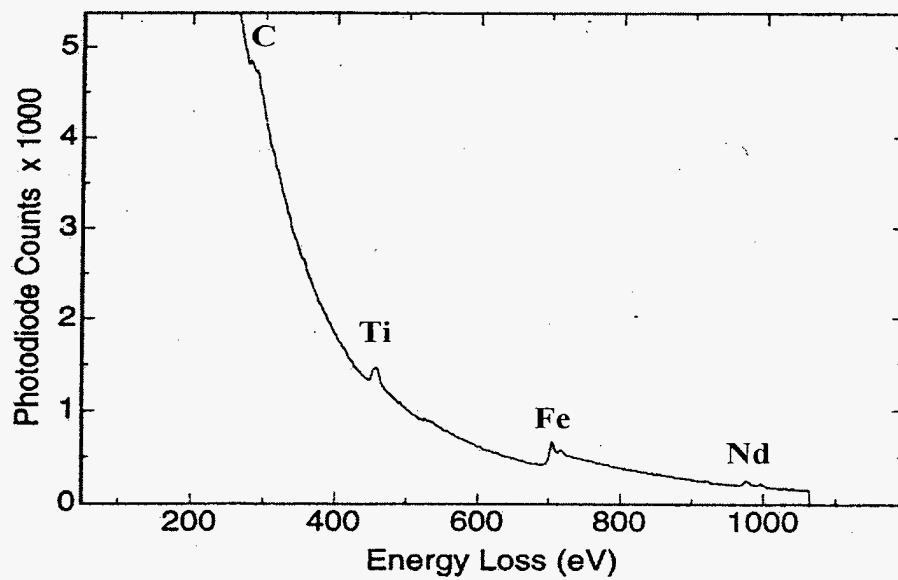
(a)

Special attention was paid to the appearance of Ti and C to study their affect on the solidification process. The appearance and the size of TiC compound is both initial composition and quenching rate dependent, it is only observed in under or optimally quenched samples with larger amount of TiC addition (3 at. % TiC for example), and TiC particles are typically 5-10 nm in size and reside in the intergranular regions instead of inside 2-14-1 grains. In over-quenched ribbon samples, only amorphous matrix and 2-14-1 nuclei have been observed, no trace of TiC compound is present, which indicates that within the quenching rates generally achieved in the melt spinning process, 2-14-1 phase is more favorable in the phase selection than the TiC compound. In addition, TiC compound is rarely observed in 2 at % TiC added ribbons melt spun from 10 m/s to 40 m/s, and a study on TiC concentration distribution in ribbons melt spun at 10 m/s using PEELS reveals that although the matrix is free of Ti and C, various boundaries coexist ranging from clean (free of Ti and C), Ti-rich, C-rich, and both Ti, C-rich, as shown in Figure 27. All these results seem to support the following explanation: when cool the melt to  $T < T_p$ , nucleation and growth of 2-14-1 grains begin and push Ti, C out locally, which causes build-up of Ti and C at the solid-liquid interface, this slows down the moving speed of the 2-14-1 growth front and accounts for the intergranular presence of both the elements. TiC compound can only form in those grain boundary regions where enough amounts of Ti and C have been accumulated and time is long enough for them to combine.

DTA results (in Figure 28) show evident difference between samples with and without TiC addition. Since those exothermic peaks correspond to the crystallization events, it can be drawn directly from the figure that both the GFA and stability of 2-14-1 glass have been improved with the increase in wheel speeds or the TiC addition. If just consider



(a)



(b)

Figure 27 EELS results on grain boundaries of 2 at.% TiC added 2-14-1 ribbons melt spun at 10 m/s: (a) Ti and C free, (b) Ti rich.

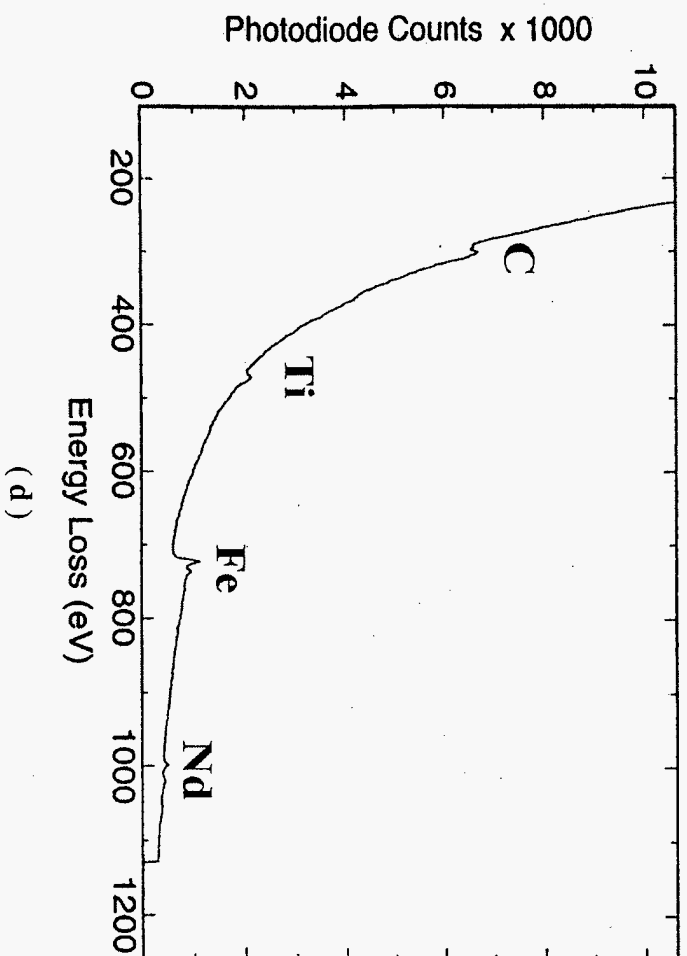
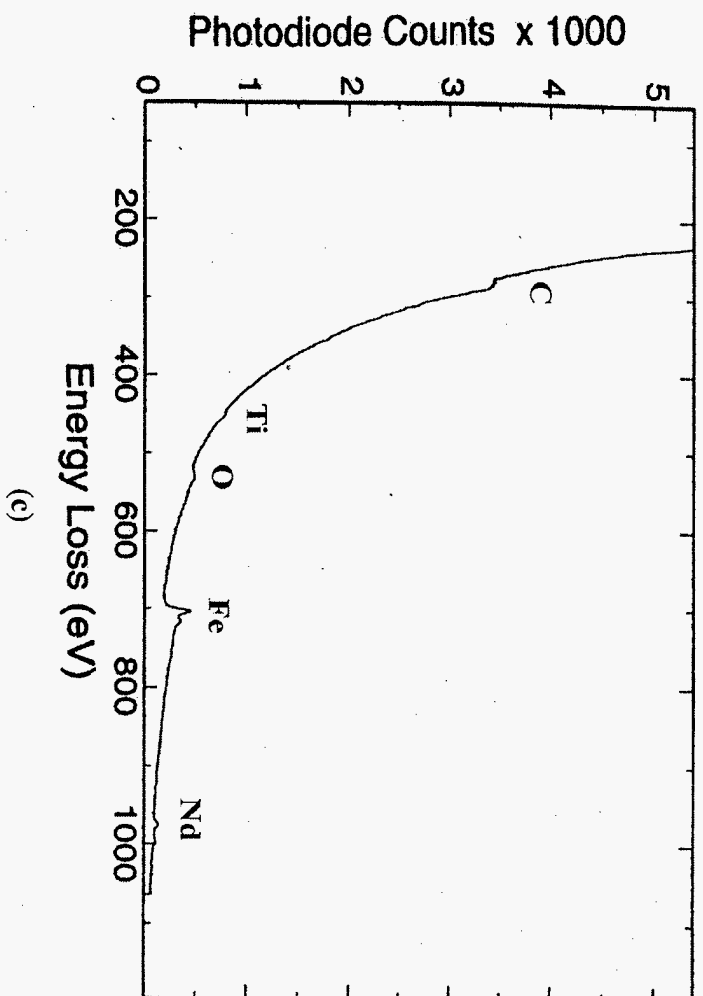


Figure 27 (continued)  
(c) C rich, (d) both Ti and C rich.

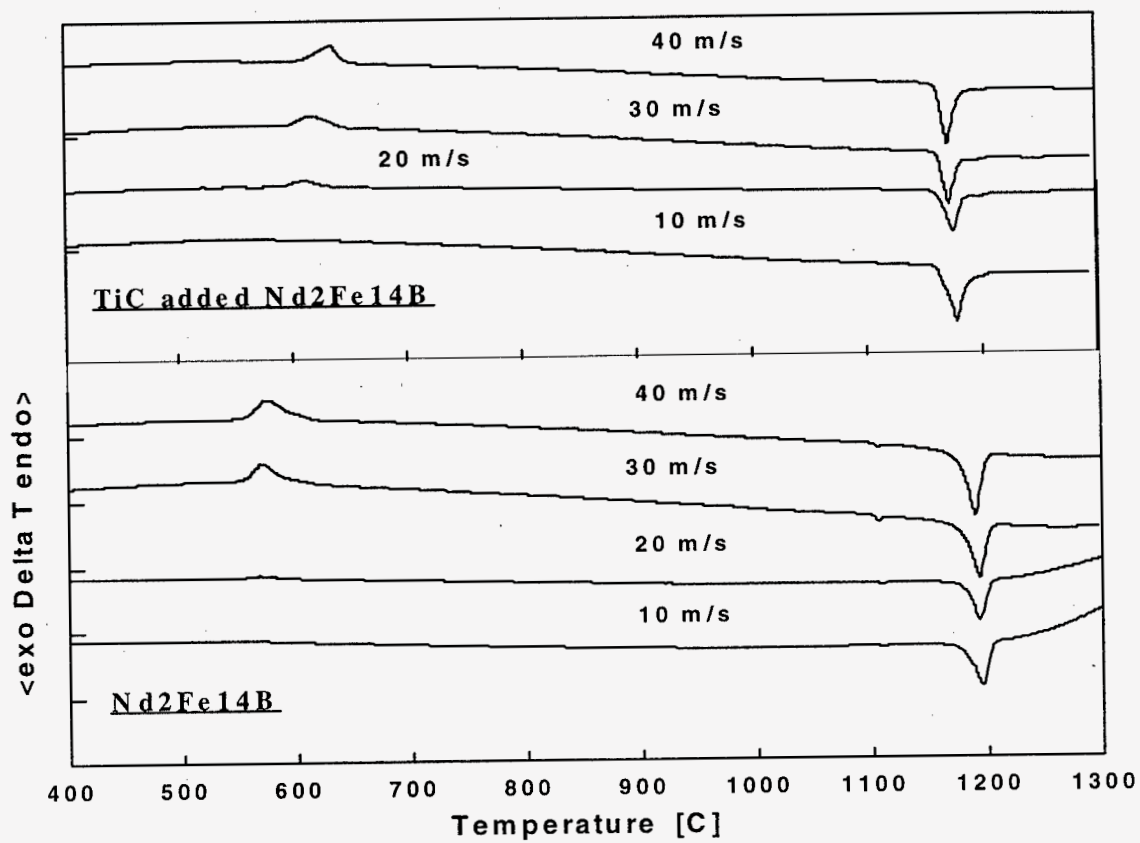


Figure 28 DTA results of 2-14-1 ribbon flakes with and without TiC addition



endothermic events, two appear in stoichiometric samples, one at  $\sim 1100^{\circ}\text{C}$  which suggests the melting of the Nd-rich intergranular phase as shown in Figure 21c, and this phase is not the eutectic  $\text{Nd}_{1.1}\text{Fe}_4\text{B}_4$  phase since its melting point is much lower ( $\sim 1010^{\circ}\text{C}$ ), the other begins at  $\sim 1180^{\circ}\text{C}$  ( $T_p$ ); only one melting event is present for all the samples with TiC addition, which occurs at a lower temperature  $\sim 1160^{\circ}\text{C}$  and has a shoulder on the right. The presence of the Nd-rich intergranular phase in 2-14-1 ribbons may attribute to the formation of free iron phase either directly through the primary reaction during the melt spinning process (under-quenched ribbons) or through crystallization process in over-quenched samples when heated during DTA measurements. In both the cases, the Nd-rich phase has to be formed to meet the stoichiometry in composition. However, when TiC is added to the system, the free iron phase is to some degree inhibited in the tested quenching region, and so-formed microstructure is almost free of Fe phase and also the Nd-rich phase. The earlier occurrence of the melting event with TiC addition may be explained by considering the interaction between 2-14-1 and TiC, if consider them as a two-component system whose phase diagram has a eutectic reaction at a certain TiC composition. It is therefore possible that the addition of TiC lowers the peritectic temperature  $T_p$  compared to the pure  $\text{Nd}_2\text{Fe}_{14}\text{B}$ .

A schematic Isothermal Transformation (IT) diagram (in Figure 29) can be further used to explain TiC's effect on the solidification process. In the diagram, solid line is the IT curve for stoichiometric  $\text{Nd}_2\text{Fe}_{14}\text{B}$  and dashed line corresponds to TiC added  $\text{Nd}_2\text{Fe}_{14}\text{B}$ . As can be seen from the diagram, TiC may actually shift the IT curve of the primary and the peritectic reactions right and down. A reason for shifting right may lie in the sluggish diffusion of Ti and C when added to the system, which increases the preparation time for the

nucleation and also slows down the growth, and the downward shifting is consistent with the lowering of  $T_p$  as measured in DTA. The shift of the IT curve can thus be used to explain the less amount of primary Fe formed.

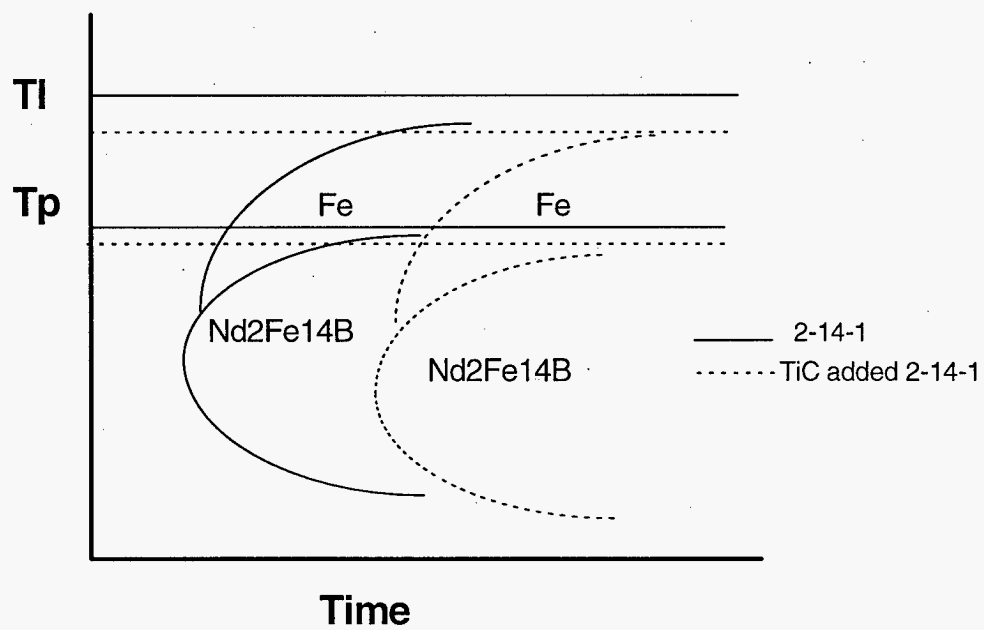


Figure 29 Schematic IT curves for 2-14-1 with and without TiC addition

## CONCLUSIONS

A generalized solidification model has been developed based on a systematic investigation on the microstructure of the melt spun Nd-Fe-B alloys. The microstructure is highly variable across the thickness of under-quenched ribbons. Although only equiaxed 2-14-1 grains are formed, their size changes from fine to very coarse from the wheel side to the free side, which is separated by a sinusoid-like shaped boundary. This boundary is pushed away from the wheel side with the increase in wheel speeds, and it disappears at about 20 m/s accompanying to the occurrence of the optimally quenched microstructure. The optimally quenched microstructure shows a surprising uniformity in the size of fine equiaxed 2-14-1 grains across the ribbon thickness, along which a positive temperature gradient is generally considered. Further increase of the wheel speed produces the over-quenched microstructure consisting of fine equiaxed and amorphous 2-14-1, and amorphous matrix is eventually formed doped with some 2-14-1 nuclei occasionally in the region close to the free side.

A generalized model modified by the dendritic breakup during recalescence was proposed to explain the solidification process, which is categorized according to the degree of undercooling achieved just before nucleation (measured here by the initial undercooled temperature  $T$ ) into the following three cases:

(1)  $T_p < T < T_1$ , the solidification process begins with the primary reaction  $L \rightarrow \alpha$ , and  $\beta$  phase nucleates later from the primarily solidified  $\alpha$  phase through the reaction  $L + \alpha \rightarrow \beta$ . Growth of the  $\beta$  phase needs to continuously transport iron atoms across the  $\alpha/\beta$  interface and consume the  $\alpha$  phase, resulting in microstructures with  $\alpha$  corings (inclusions)

inside  $\beta$  grains. Therefore, the primary solidification of  $\alpha$  phase brings diversity into the microstructures that may form. If  $\alpha$  phase nucleates heterogeneously (the initial undercooled temperature is higher than the homogeneous nucleation temperature of  $\alpha$  phase but lower than its heterogeneous nucleation temperature,  $T_n^{ho}(\alpha) < T < T_n^{he}(\alpha)$ ), the  $\alpha$  nuclei will grow dendritically or columnarly along the direction of the temperature gradient and become dendritic (or columnar) inclusions eventually. Because of the positive temperature gradient across the melt spun ribbons, alignment of these primarily solidified  $\alpha$  dendrites may be achieved and thus so-formed microstructure may be textured. If copious homogeneous nucleation of the  $\alpha$  phase, which is caused by impurity and compositional fluctuation in the melt, becomes dominant due to larger undercoolings,  $T_p < T < T_n^{ho}(\alpha)$  for example, thus microstructures with spherical (or particular)  $\alpha$  corings may form.

(2)  $T_g < T < T_p$ ,  $\beta$  phase nucleates first and the primary solidification is inhibited (or suppressed). If the cooling rate is not very fast ( $T_n^{ho}(\beta) < T < T_n^{he}(\beta)$ ),  $\beta$  phase will nucleate heterogeneously and grow. The growth front of the  $\beta$  phase can move very rapidly so that the heat of crystallization released exceeds the heat dissipation rate through the solid layer and the interface with the wheel. The temperature of the material then starts to rise, which is referred as recalescence. The recalescence causes the temperature of the solidified part higher than the front liquid and produces a negative temperature gradient across the solidification front which favors dendritic growth. If the maximum temperature during the recalescence  $T_r$  is lower than the peritectic temperature  $T_p$ , or even if  $T_r > T_p$  but the time remaining on the quasistatic plateau is not long enough to break up the  $\beta$  dendrites, columnar (dendritic)  $\beta$  phase initially formed remains. Otherwise, these dendrites break up into fine segments and

based on which a fine equiaxed microstructure is later formed. Meanwhile, nucleation of the  $\alpha$  phase can occur in the interdendritic regions, and this phase can grow into small particles residing in  $\beta$  grain conjunctions.

If the cooling is very fast, which means  $T_g < T < T_n^{ho}(\beta)$ ,  $\beta$  phase may homogeneously nucleate in the bulk or  $\beta$  nuclei do not have enough time to grow, equiaxed or spherical 2-14-1 may form in a glassy matrix.

(3)  $T < T_g$ , glass begins to form wherever  $T < T_g$ , and the lower the temperature that the melt has been suppressed nucleation, the more stable the glass that has formed.

The solidification process in the melt spinning of 2-14-1 alloys can thus be explained using the above categorized solidification model. The solidification of an under-quenched ribbon begins from the wheel side where  $T < T_p$ , precisely  $T_p^{ho} < T < T_p^{he}$ , and thus 2-14-1 phase heterogeneously nucleates from the wheel surface and grows dendritically across the ribbon, this is one growth front. Meanwhile, there is another growth front of free iron phase due to the fact that the initial undercooled temperature somewhere inside the ribbon is higher than  $T_p$  and the primary solidification of the free iron phase is preferred, which grows dendritically (or columnarly) toward the free surface. The recalescence has raised temperature of the first region to  $T_r > T_p$  and stayed long enough to break the 2-14-1 dendrites, and fine equiaxed 2-14-1 grains later form on these dendritic segments during cooling below  $T_p$ , also during the recalescence secondary free iron phase may form and resides at grain conjunctions. The region beginning with free iron phase has developed coarse 2-14-1 grains with free iron dendritic inclusions. With the increase in wheel speeds, both the wheel side temperature and the slope of the temperature profile at the onset of the nucleation decrease. For ribbons melt

spun at 20 m/s, most of the melt has been undercooled to  $T < T_p$  before the occurrence of nucleation, though a thermal gradient still exists across the ribbon thickness, only one growth front of the 2-14-1 phase exists. Heterogeneous 2-14-1 nucleation begins from the wheel surface and grows dendritically through the whole ribbon. These dendrites break up during recalescence and a uniform equiaxed microstructure is formed as described before. Also the breaking up of 2-14-1 dendrites during the recalescence is always accompanied by the formation of the secondary free iron phase. The 30 m/s wheel speed suppresses the wheel side initial undercooled temperature below the glass forming temperature  $T_g$ , and substantial amount of glassy 2-14-1 forms adjacent to the wheel side. However, there is a region close to the free side where  $T_p > T > T_g$ , precisely  $T_n^{ho} > T > T_g$ , where homogeneous nucleation of the 2-14-1 phase occurs, and because of rapid heat extraction rate at this high wheel speed, temperature cools down below  $T_g$  before this region is fully crystallized and some glass remains at intergranular regions. When the wheel speed reaches 40 m/s, almost all parts of each ribbon have been undercooled to  $T < T_g$  and featureless glassy matrix is formed throughout the whole ribbon. Meanwhile, the amorphous 2-14-1 formed in 40 m/s ribbons is more viscous than the glass formed at 30m/s because of larger degree of undercooling achieved.

C-axis texturing study is an application of the first case in our generalized solidification model. The investigation reveals that the coarse 2-14-1 grains with dendritic Fe inclusions on the free side of the under-quenched ribbons are aligned with the c-axis normal to the ribbon surface, and also a epitaxy seems present between the Fe dendritic inclusions and their host 2-14-1 grain with  $(110)_{\alpha-Fe} // (330)_{2-14-1}$  and  $[1-11]_{\alpha-Fe} // [001]_{2-14-1}$ . The texturing

phenomenon suggests the same solidification sequence as described in the first case, the primary solidification occurs prior to the peritectic solidification, and the origin of the texturing was explained based on the model as the alignment of the primarily solidified Fe dendrites and the epitaxy between the Fe and the 2-14-1. Two lines of investigation based on TEM and XRD were further conducted to test the factors that may affect the primary Fe dendritic growth and its alignment (the temperature gradient), these factors including the shooting temperature, the wheel speed, the composition, the wheel material and TiC addition all change the degree of the c-axis alignment in such a way that is consistent with our explanation. A maximum degree of the alignment is reached at an optimum wheel speed which is determined by the particular quenching characteristic and reflects a compromise between the alignment of the primarily solidified Fe dendrites and the coverage of the regions beginning with the primary solidification.

As an extension of our model, the solidification of TiC added 2-14-1 has also been investigated. Ti and C addition seems to slow the growth fronts of both the primary Fe and the 2-14-1 due to kinetic effect. The slowing down of the 2-14-1 growth front brings finer grain size and improved Glass Forming Ability (GFA). The effect of Ti and C addition on Fe dendritic growth disturbs its alignment and no texturing has been found in TiC added under-quenched ribbons, and the so-formed Fe appears to be spherical instead of dendritic as in the stoichiometric counterpart.



## REFERENCES

- [ 1] T. Abraham, *JOM* **47**(1995), 16.
- [ 2] G. J. Long, F. Grandjean, Supermagnets, Hard Magnetic Materials, Kluwer Academic publishers, Boston, 1991.
- [ 3] J. M. D. Coey, Rare-earth Permanent Magnets, Clarendon Press. London, 1996.
- [ 4] J. J. Croat, J. F. Herbst, R. W. Lee and F. E. Pinkerton, *J. Appl. Phys.* **55**(1984), 2078.
- [ 5] M. Sagawa, S. Fujimura, N. Togawa, H. Yamamoto and Y. Matsuura, *J. Appl. Phys.* **55**(1984), 2083.
- [ 6] J. F. Herbst, *American Scientist* **81**(1993), 2.
- [ 7] J. J. Croat, *J. Mater. Eng.* **10**(1988), 7.
- [ 8] D. J. Branagan, Doctoral thesis, Iowa State University, 1995.
- [ 9] S. Tanigawa, Y. Hara and N. J. Grant et al., *IEEE Trans. Magn.* **MAG-22**(1986), 746.
- [10] K. S. V. L. Narasimhan and E. J. Dulis, *US patent N0. 4588349*(1986).
- [11] L. Schultz, J. Wecker and E. Hellstern, *J. Appl. Phys.* **61**(1987), 3583.
- [12] L. Schultz, K. Schnitzke and J. Wecker, *J. Magn. Magn. Mater.* **80**(1989), 115.
- [13] T. Harada, T. Ando, R. C. O'Handley and N. J. Grant, *J. Appl. Phys.* **67**(1990), 4233.
- [14] E. J. Lavernia and N. J. Grant, *Mater. Sci. Eng.* **98**(1988), 381.
- [15] B.M. Ma, V. K. Chandhok and E. J. Dulis, *IEEE Trans. Magn.* **MAG-23**(1987), 2518.
- [16] J. P. Nozieres, R. Perrier de La Bathie and D. W. Taylor, *J. Magn. Magn. Mater.* **80**(1989), 88.

- [17] T. Shimoda, K. Akioka, O. Kobayashi and Y. Yamagami, *J. Appl. Phys.* **64**(1988), 5290.
- [18] T. Ohki and T. Yuri, *IEEE Trans. Magn.* **MAG-29**(1993), 2800.
- [19] P. J. McGuinness, X. J. Zhang, X. J. Xin and I. R. Harris, *J. Less-Common Met.* **158**(1990), 359.
- [20] A. Hutten, *JOM* **44**(1992), 11.
- [21] J. Ormerod, *J. Less-Common Met.* **111**(1985), 49.
- [22] V. Panchanathan, *J. Mater. Eng. Perf.* **4**(1995), 423.
- [23] R. Coehoorn and J. Duchateau, *Mater. Sci. Eng.* **99**(1988), 137.
- [24] S. Hirose, A. Hanaki, H. Tomizawa and A. Hamamura, *Physica B* **164**(1990), 117.
- [25] D. R. Gander, M. H. Fronig, R. J. White and A. E. Ray, *J. Appl. Phys.* **63**(1988), 3522.
- [26] M. Pont, J. Reverter and J. S. Munoz, *IEEE Trans. Magn.* **MAG-29**(1993), 2797.
- [27] Yu. M. Rabinovich, S. Szymura, J. J. Wyslocki and H. Bala, *J. Magn. Magn. Mater.* **140-144**(1995), 1065.
- [28] M. Zhang, D. Ma, X. Jiang and S. Liu, 8<sup>th</sup> Int. Workshop on Rare Earth -Magnets and Their Applications, Dayton, 1985, 541.
- [29] C. Abache and H. Oesterreicher, *J. Appl. Phys.* **60**(1986), 114.
- [30] P. Tenaud, F. Vial and M. Sagawa, *IEEE Trans. Magn.* **MAG-26**(1990), 1930.
- [31] W. Rodewald and B. Wall, *J. Magn. Magn. Mater.* **80**(1989), 57.
- [32] M. Tokunaga, H. Kogure, M. Endoh and H. Harada, *IEEE Trans. Magn.* **MAG-23**(1987), 2287.
- [33] G. Rieger, M. Seeger, S. Li and H. Kronmüller, *J. Magn. Magn. Mater.* **151**(1995), 193.
- [34] B.M. Ma, W. L. Liu, Y. L. Liang, D. W. Scott and C. O. Bounds, *J. Appl. Phys.* **75**(1994), 6628.

- [35] M. Sagawa, *J. Mater. Eng.* **13**(1991), 95.
- [36] K. G. Knoch, G. Schneider, J. Filder, E. -Th. Henig and H. Kronmuller, *IEEE Trans. Magn.* **MAG-25**(1989), 3426.
- [37] A. Micski and B. Uhrenius, *J. Appl. Phys.* **75**(1994), 6265.
- [38] M. Tokunaga, Y. Nozawa, K. Iwasaki, S. Tanigawa and H. Harada, *J. Magn. Magn. Mater.* **80**(1989), 80.
- [39] Y. Kitano, J. Shimomura and M. Shimotomai, *J. Appl. Phys.* **69**(1991), 6055.
- [40] D. J. Branagan and R. W. McCallum, *J. Magn. Magn. Mater.* **146**(1995), 89.
- [41] K. Fritz, B. Grieb, E. -T. Henig and G. Petzow, *Z. Metallkd.* **83**(1992), 157.
- [42] L. Withanawasam, A. S. Murthy and G. C. Hadjipanayis, *IEEE Trans. Magn.* **MAG-31**(1995), 3608.
- [43] A. Manaf, M. A. Khafaji, P. Z. Zhang, H. A. Davis, R. A. Buckley and W. M. Rainforth, *J. Magn. Magn. Mater.* **128**(1993), 307.
- [44] A. Inoue and A. Takeuchi, A. Makino and T. Masumoto, *IEEE Trans. Magn.* **MAG-31**(1995), 3626.
- [45] R. K. Mishra, *J. Magn. Magn. Mater.* **54-57**(1986), 450.
- [46] J. Fidler and K. G. Knoch, *J. Magn. Magn. Mater.* **80**(1989), 48.
- [47] S. Hirosawa and Y. Tsubokawa, *J. Magn. Magn. Mater.* **84**(1990), 309.
- [48] W. Grunberger, M. Schmidt and B. Springmann, *IEEE Trans. Magn.* **MAG-30**(1994), 636.
- [49] R. K. Mishra, *J. Appl. Phys.* **62**(1987), 967.
- [50] G. P. Meisner, V. Panchanathan, *J. Appl. Phys.* **74**(1993), 3514.
- [51] A. Hutten and G. Thomas, *Ultramicroscopy* **47**(1992), 447.
- [52] A. Higuchi and S. Hirosawa, *IEEE Trans. Magn.* **MAG-25**(1989), 3555.
- [53] J. F. Herbst, *Rev. Mod. Phys.* **63**(1991), 819.

- [54] S. Chikazuma, *J. Magn. Magn. Mater.* **54-57** (1986), 1551.
- [55] J. D. Livingston, *J. Appl. Phys.* **57**(1985), 4137.
- [56] F. E. Pinkerton and D. J. van Wingerden, *J. Appl. Phys.* **60**(1986), 3685.
- [57] G. C. Hadjipanaylis, R. C. Dickenson and K. R. Lawless, *J. Magn. Magn. Mater.* **54-57** (1986), 557.
- [58] M. Sato, Y. Ishii, *J. Appl. Phys.* **66**(1989), 983.
- [59] E. D. Samwell, P. R. Bissell, J. C. Lodder, *J. Appl. Phys.* **73**(1993), 1353.
- [60] J.J. Croat and J. F. Herbst, MRS Bulletin, June 1990, 37.
- [61] P.R. Sahm, H. Jones and C. M. Adam, Science and Technology of the Undercooled Melt, Martinus Nijhoff Publishers, 1986.
- [62] M. Prates and H. Boloni, *Met. Trans.* **3**(1972), 1501.
- [63] R. B. Pond and J. M. Winter, *AIChE Symposium series* **180**(1978), 98.
- [64] A. Zaluska, Yan Xu, Z. Altounian, and R. Allem et al., *J. Mater. Res.* **6**(1991), 724.
- [65] D. Lemarchand, F. Vial, A. Hauet, B. Labulle and P. Vigier, *IEEE Trans. Magn.* **26**(1990), 253.
- [66] M. Schwarz, A. Karma, K. Eckler and D. M. Herlach, *Phys. Rev. Lett.* **73** (1994), 1380.
- [67] A. L. Greer, *Mater. Sci. Eng.* **A133**(1991), 16.
- [68] A. Munitz and G. J. Abbaschian, Undercooled Alloy Phases, The Metallurgy Society, Warrendale, 1986, 23.
- [69] M. J. Kramer, C.P. Li and R.W. McCallum et al., *J. Appl. Phys.* **81**(1997), 1.
- [70] R. W. McCallum and M. J. Kramer(personal communication).
- [71] D. J. Branagan, T. A. Hyde, C. H. Sellers and R. W. McCallum, *J. Phys. D: Appl. Phys.* **29**(1996), 2376.
- [72] J. Yamasaki, A. Furuta and Y. Hirokado, *IEEE Trans. Magn.* **MAG-25**(1989), 4120.

- [73] D. Dadon, Y. Gefen and M. P. Dariel, *IEEE Trans. Magn.* **MAG-23**(1987), 3605.
- [74] D. Akhtar, T. Spassov and U. Koster, *Z. Metall.* **Bd 82**(1991), 823.
- [75] P. Tenaud, A. Chamberod and F. Vanoni, *Solid State Commun.* **63**(1987), 303.

## ACKNOWLEDGEMENTS

This thesis is dedicated to my wife, Jiang Yun. Without her love and support, her belief in me, I could not possibly achieved what I have done here. Also thanks to my parents who have inherited me the sense of hard working and self respect.

I am fortunate to work under the guidance of Dr. Bill McCallum and Dr. Matt Kramer. With his experience in this field, Bill not only guided me out of messy data, but also taught me how to do research and to be professional. The core of this work could not possibly have been done without valuable help from Matt. His patience and mastery of TEM technique inspired me through my staying here and will last all my life. Though I have not learned enough from Matt (maybe never will), the TEM pictures and other data in this thesis show my appreciation to him.

Thanks to Kevin Dennis, who helped me set up experiments and saved my enormous amount of time. Fran Laabs and Scott Chumbley are appreciated for helping me with the TEM techniques and keeping devices running nicely.

I have made many friends that have helped me along the way. Those that especially come to mind are Carl Schwichtenberg, Henning Wu, Jing Zheng, Larry Margulies, Liugui Zhong and Tone Lund, and former group memder Dan Branagan and Jeff Shield.

This work was performed at Ames Laboratory under Contract No. W-7405-Eng-82 with the U.S. Department of Energy. The United States government has assigned the DOE Report number IS-T 1833 to this thesis.

M98004653



Report Number (14) IS-T--1833

Publ. Date (11) 19980223

Sponsor Code (18) DOE/ER, XF

UC Category (19) UC-400, DOE/ER

DOE